Stem Cell Reports
Article

ISSCR

OPEN ACCESS

Organoids from mouse molar and incisor as new tools to study tooth-specific biology and development

Florian Hermans,[1,2] Lara Hemeryck,[2] Celine Bueds,[2] Marc Torres Pereiro,[2] Steffie Hasevoets,[1] Hiroto Kobayashi,[3] Diether Lambrechts,[4,5] Ivo Lambrichts,[1] Annelies Bronckaers,[1,6,*] and Hugo Vankelecom[2,6,*]

[1]Department of Morphology, Biomedical Research Institute, Faculty of Medicine and Life Sciences, Hasselt University, 3590 Diepenbeek, Belgium
[2]Laboratory of Tissue Plasticity in Health and Disease, Cluster of Stem Cell and Developmental Biology, Department of Development and Regeneration, KU Leuven (University of Leuven), 3000 Leuven, Belgium
[3]Department of Anatomy and Structural Science, Yamagata University Faculty of Medicine, Yamagata, Japan
[4]Center for Cancer Biology, VIB, 3000 Leuven, Belgium
[5]Laboratory for Translational Genetics, Department of Human Genetics, KU Leuven, 3000 Leuven, Belgium
[6]Senior author
*Correspondence: annelies.bronckaers@uhasselt.be (A.B.), hugo.vankelecom@kuleuven.be (H.V.)
https://doi.org/10.1016/j.stemcr.2023.03.011

SUMMARY

Organoid models provide powerful tools to study tissue biology and development in a dish. Presently, organoids have not yet been developed from mouse tooth. Here, we established tooth organoids (TOs) from early-postnatal mouse molar and incisor, which are long-term expandable, express dental epithelium stem cell (DESC) markers, and recapitulate key properties of the dental epithelium in a tooth-type-specific manner. TOs display *in vitro* differentiation capacity toward ameloblast-resembling cells, even more pronounced in assembloids in which dental mesenchymal (pulp) stem cells are combined with the organoid DESCs. Single-cell transcriptomics supports this developmental potential and reveals co-differentiation into junctional epithelium- and odontoblast-/cementoblast-like cells in the assembloids. Finally, TOs survive and show ameloblast-resembling differentiation also *in vivo*. The developed organoid models provide new tools to study mouse tooth-type-specific biology and development and gain deeper molecular and functional insights that may eventually help to achieve future human biological tooth repair and replacement.

INTRODUCTION

In the last decade, organoid technology has proven to be a powerful tool to explore tissue biology and development (Clevers, 2016; Boretto et al., 2017; Artegiani and Clevers, 2018; Cox et al., 2019; Hemeryck et al., 2022). Tissue-derived organoids develop when tissue (stem) cells or fragments are embedded in a 3D extracellular matrix scaffold (typically Matrigel) and exposed to a defined growth factor cocktail that replicates key tissue stem cell niche and developmental signaling factors. These organoid models closely recapitulate phenotypical and functional characteristics of the tissue of origin, much better than traditional 2D cell cultures, and they are highly and long-term expandable with preservation of their characteristics (Clevers, 2016; Hemeryck et al., 2022). Importantly, these stem cell organoids are able to differentiate into specific tissue cell types following exposure to differentiation factors or co-culture with other cell types (Artegiani and Clevers, 2018).

Although *in vivo* experiments using genetically modified mice have provided important insights into mouse tooth development and biology, deep knowledge is still missing, particularly regarding overlap or distinctions between molars and incisors, largely due to a lack of reliable and tractable *in vitro* models. Previous cell culture models of mouse dental epithelium (DE) cells, including 2D immortalized, non-physiological cell lines, 2D pluripotent stem cell-derived DE-like cells, and 3D (incisor) spheroids or tooth germ aggregates, lack the important assets of tissue-derived organoids such as faithful recapitulation of tissue-specific phenotype and function and robust long-term expandability (Nakao et al., 2007; Sarkar et al., 2014; Binder et al., 2020; Miao et al., 2022). Moreover, many of the previous models were derived from only one tooth type, thus not allowing decipherment of molar- and incisor-specific biology and development.

In this study, we report the establishment of organoid models starting from both mouse molar and incisor. The obtained epithelial organoids are long-term expandable, recapitulate tooth-specific characteristics, and show dental epithelium stem cell (DESC) differentiation properties, both *in vivo* and *in vitro*, the latter further reinforced by the presence of dental mesenchymal (pulp) stem cells, thereby mirroring the important epithelial-mesenchymal crosstalk as occurring during tooth development.

Taken together, our study provides a new powerful tool to explore and contrast mouse molar and incisor biology and development. Together with our recently developed human tooth-derived organoid model (Hemeryck et al., 2022), the here established mouse tooth organoids (TOs) form a highly valuable arsenal of *in vitro* research tools to decipher tooth biology and development and to open translational

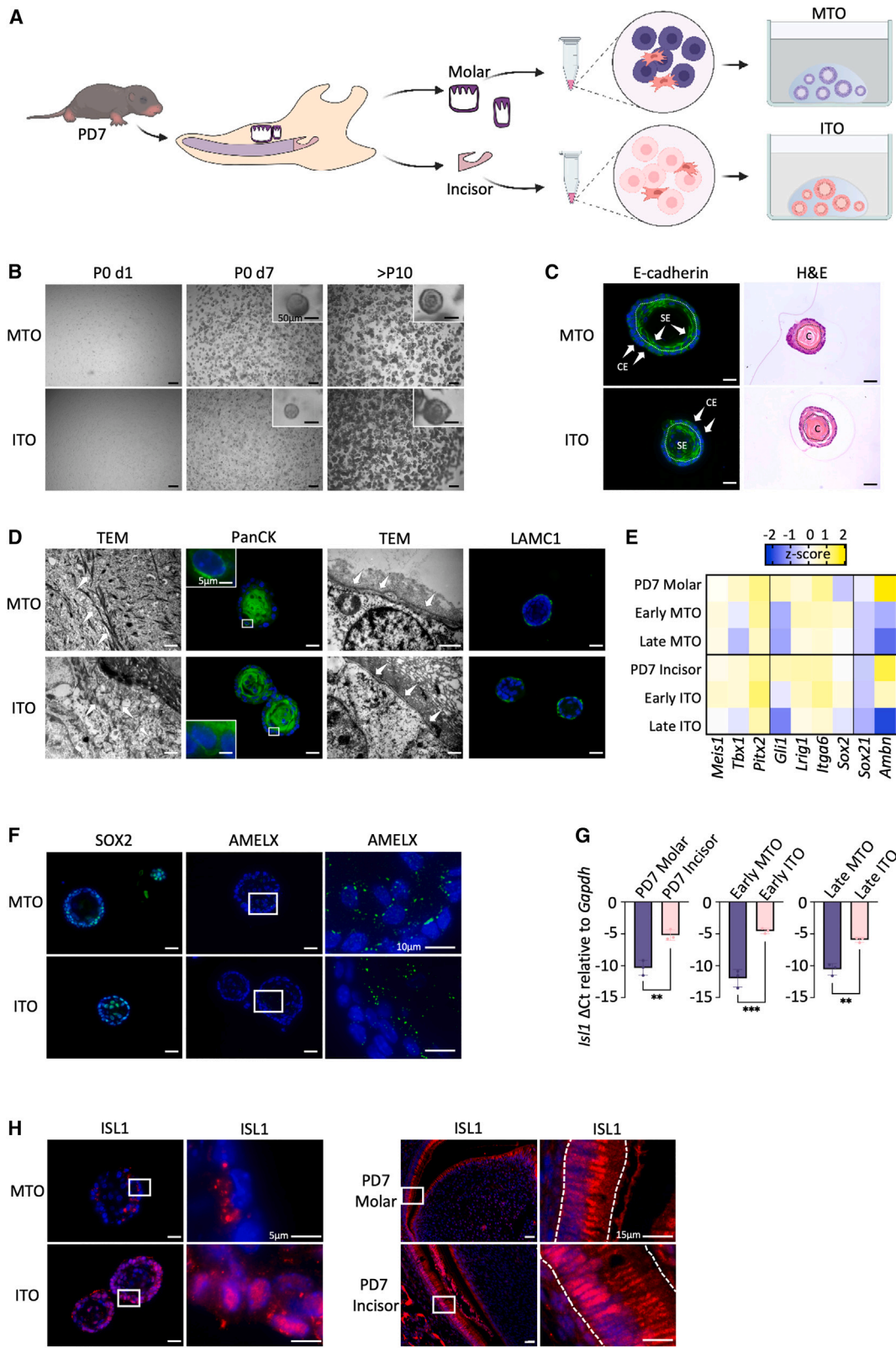

(legend on next page)

perspectives toward tooth repair and replacement, envisioned to eventually be instrumental to counter and cure the highly prevalent and burdening tooth pathologies.

RESULTS

Establishing organoids from mouse molar and incisor

To establish mouse epithelial TOs, we dissected developing (unerupted) teeth from early-postnatal (i.e., postnatal day 7, PD7) mice and isolated the dental epithelium and attached dental follicle from molars and the DESC-containing apical ends from incisors (Figure 1A). Following enzymatic and mechanical trituration, the cell mixture was seeded in Matrigel droplets and cultured in a precisely defined medium, designated as "tooth organoid medium" (TOM), encompassing key stem cell niche factors previously identified to enable development and growth of human tooth organoids (Hemeryck et al., 2022). In particular, canonical organoid (stem cell) growth and differentiation-inhibiting factors such as wingless-type MMTV integration site (WNT) activators (R-spondin 1 [RSPO1] and WNT3A), bone morphogenetic protein (BMP) inhibitor (Noggin), p38 mitogen-activate protein kinase (MAPK) inhibitor (SB202190), and transforming growth factor β (TGFβ) inhibitor (A83-01) and more specific (dental) stem cell niche regulatory growth factors such as sonic hedgehog (SHH), fibroblast growth factors (FGF), and insulin-like growth factor-1 (IGF1) are included in the TOM (for exact composition, see Tables 1 and S1). Notably, our previously defined TOM did not need epidermal growth factor (EGF) (Hemeryck et al., 2022), which is peculiar since it is a prototypical component in nearly all organoid media.

Organoids swiftly develop from both molar and incisor tissue (referred to as molar TO [MTO] and incisor TO [ITO]) and can be stably expanded and long-term passaged, at present for more than 10 passages (i.e., longer than 3 months; Figure 1B). Both MTOs and ITOs are epithelial in nature (as shown by E-cadherin expression) and display a dense morphology with an outer layer of cuboidal epithelium, an intermediate layer of stratified epithelium, and a dense inner core (Figure 1C). Moreover, the TOs are characterized by an abundance of cytokeratin (CK) filaments, especially in the core region with lower level in the periphery, as shown by transmission electron microscopy (TEM) and CK immunoreactivity (including CK5, CK14, and CK8/18; Figures 1D and S1A). Desmosomes, which play an important role in anchoring CK filaments and mediating cell-cell adhesion, are also abundantly detected in the TO, especially toward the CK-rich core region (TEM and desmoglein 1 [DSG1] immunoreactivity; Figure S1B). Both organoid types are boarded by laminin-containing basement membrane (TEM and laminin subunit gamma 1 [LAMC1] immunoreactivity; Figure 1D), indicating organoid polarity.

Interestingly, both MTOs and ITOs express key transcription factors (TFs) involved in the development of the DE (e.g., *Meis1*, *Tbx1*, and *Pitx2*), as well as proposed DESC markers (e.g., *Gli1*, *Lrig1*, *Itga6*, and the well-established *Sox2*/SOX2) (Figures 1E and 1F), all as found in the primary tissue (Figure 1E) (Catón et al., 2009; Sanz-Navarro et al., 2019; Hermans et al., 2021). Overall, these markers remain expressed in late-passage (P6) TOs (Figure 1E). However, lower levels of ameloblast (AB) markers such as the TF *Sox21* and the enamel matrix proteins (EMPs) *Ambn, Odam*, and *Amtn* are observed when compared with early-passage TOs (i.e., immediately after seeding; P0) (Figure 1E),

Figure 1. Development and characterization of organoids from mouse molar and incisor

(A) Schematic of experimental setup for derivation of TOs from early-postnatal (PD7) mouse molar and incisor.

(B) Progressive development (bright-field pictures) of TOs after initial seeding (passage 0 (P0) day 1 (d1)), 7 days after initial seeding (P0 d7), and after long-term culture for more than 10 passages (>P10). Magnified view is in boxes.

(C) Immunofluorescence (IF) and histological (H&E) analysis of TO phenotype and morphology. Regarding E-cadherin IF (green), arrows indicate outer layer cuboidal epithelium (CE) or inner layer stratified epithelium (SE). Nuclei are counterstained with Hoechst33342 (blue; for all IF images). Delineation between layers is indicated by white dotted line. Black dotted line delineates the centrally localized core region in H&E.

(D) Ultrastructural (TEM) and IF (of indicated markers) characterization of TO. Arrows indicate keratin filaments (left TEM images) or outer basement membrane (right TEM images). Boxed areas are magnified.

(E) Heatmap of gene expression of DE TFs, proposed DESC markers, and EMPs in primary molar and incisor tissue (PD7) and early- and late-passage TOs, as quantified by qRT-PCR analysis. Data are presented as relative expression to *Gapdh* (ΔC_t) and *Z* score normalized. Colors range from blue (low expression) to yellow (high expression).

(F) IF analysis of SOX2 and AMELX in TOs (green). Boxed areas are magnified.

(G) Bar graph (mean ± standard error of the mean [SEM]) showing expression of *Isl1* relative to *Gapdh* (ΔC_t) for primary molar and incisor tissue (left), early-passage TOs (middle), and late-passage TOs (right). Data points represent biological replicates from independently obtained primary tissue and independently established organoid lines; unpaired t test.

(H) IF analysis of ISL1 in TOs and primary molar and incisor. Boxed areas are magnified.

Scale bars: 250 μm for bright-field images, 25 μm for IF and H&E images, and 1 μm for TEM images, unless indicated otherwise. $^{**}p < 0.01$, $^{***}p < 0.001$. See also Figure S1.

Table 1. Tooth organoid medium (TOM) composition

Product	Concentration	Supplier	Catalog number
Serum-free defined medium (SFDM)			For composition, see Table S1
A83-01	0.5 μM	Sigma-Aldrich	SML0788
B27 (without vitamin A)	1X	Gibco	12587-010
Cholera toxin	100 ng/mL	Sigma-Aldrich	C8052-.5mg
FGF2 (=basic FGF)	20 ng/mL	R&D Systems	234-FSE
FGF8	200 ng/mL	Peprotech	AF-100-25
FGF10	100 ng/mL	Peprotech	100-26
L-glutamine	2 mM	Gibco	25030081
IGF1	100 ng/mL	Peprotech	100-11
N2	1X	Gibco	17502-048
N-acetyl L-cysteine	1.25 mM	Sigma-Aldrich	A7250
Nicotinamide	10 mM	Sigma-Aldrich	N0636
Noggin	100 ng/mL	Peprotech	120-10C
RSPO1	200 ng/mL	Peprotech	120-38
SB202190	10 μM	Biotechne (Tocris)	1264
SHH	100 ng/mL	R&D Systems	464-SH
WNT3A	200 ng/mL	R&D Systems	5036-WN
EGF[a]	20 ng/ML	R&D Systems	236-EG

[a]For all results from Figure 3 onward, TOM was by default supplemented with EGF.

which is most likely due to the disappearance of certain seeded cell types (such as AB) at further passaging in typical organoid culture conditions (Fujii and Sato, 2020; Saito et al., 2020; Hemeryck et al., 2022). Moreover, as also found before in human TOs and present in developing DESCs (Hemeryck et al., 2022), the EMP AMELX was detected in the mouse TOs in its typical punctuated pattern (Figure 1F).

Of note, ISL LIM homeobox 1 (ISL1) is known as a key TF involved in development of the incisor DE (Naveau et al., 2017). Accordingly, we find higher gene expression in PD7 incisor than molar. Interestingly, this expression difference is faithfully recapitulated in the organoids (early and late passage; Figure 1G). This observation was further validated by immunofluorescence analysis (Figure 1H) (Naveau et al., 2017). In ITOs, ISL1 is found in the majority of cells where it is localized in both nucleus and cytoplasm, whereas in MTOs, ISL1 is detected in only a few cells, being localized in the cytoplasm. Interestingly, these findings match the *in vivo* situation; in incisors, ISL1 is abundantly observed in the nuclei (and cytoplasm) of the majority of ABs, whereas in molars, it is detected only in the cytoplasm of the densely packed molar ABs. Our findings show that MTOs and ITOs retain tooth-specific transcriptional programs. In further support, principal component analysis (PCA) of bulk RNA-sequencing (RNA-seq) data generated from both TO types reveals clustering of the organoids based on their tooth of origin (Figure S1C). Moreover, this RNA-seq analysis confirmed incisor-specific expression of *Isl1* in ITOs and identified molar-specific expression of *Irx1* and *Irx2* in MTOs, and both findings were further validated in primary mouse tooth tissue by applying our recently published single-cell RNA-seq (scRNA-seq) atlas (Figures S1D and S1E) (Hermans et al., 2022).

Taken together, we successfully established epithelial organoids from early-postnatal mouse molar and incisor that recapitulate key (tooth-specific) phenotypic DE features.

Differential response of MTOs and ITOs to exogenous EGF exposure, recapitulating *in vivo* behavior

Intriguingly, EGF, typically needed to establish organoids from tissues, is not essential for mouse TO development and passaging, in line with our recent observation in organoid development from human tooth (Hemeryck et al., 2022). However, when EGF is supplemented to the established TOM, the size of ITOs increases, although MTO diameter is not affected (Figure 2A). In accordance, proliferative activity (as analyzed by EdU incorporation) is significantly augmented in ITOs when exposed to EGF but not in MTOs (Figure 2B). Of note, basal proliferation of MTOs (i.e., in TOM without EGF) is higher than of ITOs (Figure 2B). Both organoid types can be maintained long-term in the presence of EGF, comparable to culturing without EGF, and retain similar morphological and phenotypical characteristics, including expression of E-cadherin, SOX2, and AMELX, and reduced *Isl1* expression in MTOs compared with ITOs (Figures S2A and S2B). Finally, we observed that the maintenance of ITO culture is facilitated with EGF, epitomized by the significantly reduced time between passaging (Figure S2C).

Differential sensitivity of MTOs and ITOs to exogenous EGF may have to do with the presence of, and differences in, endogenous EGF activity. Blocking the EGF receptor (EGFR) with a reversible (AG-1478) or irreversible (EKI-785) inhibitor in TOM (i.e., without EGF supplementation) results in a prominent reduction of MTO growth (diameter), while only marginally affecting ITO size (only with EKI-785; Figure 2C). The specificity of the inhibitors on EGFR signaling was confirmed by their inhibitory effect on organoids grown in the presence of exogenous EGF

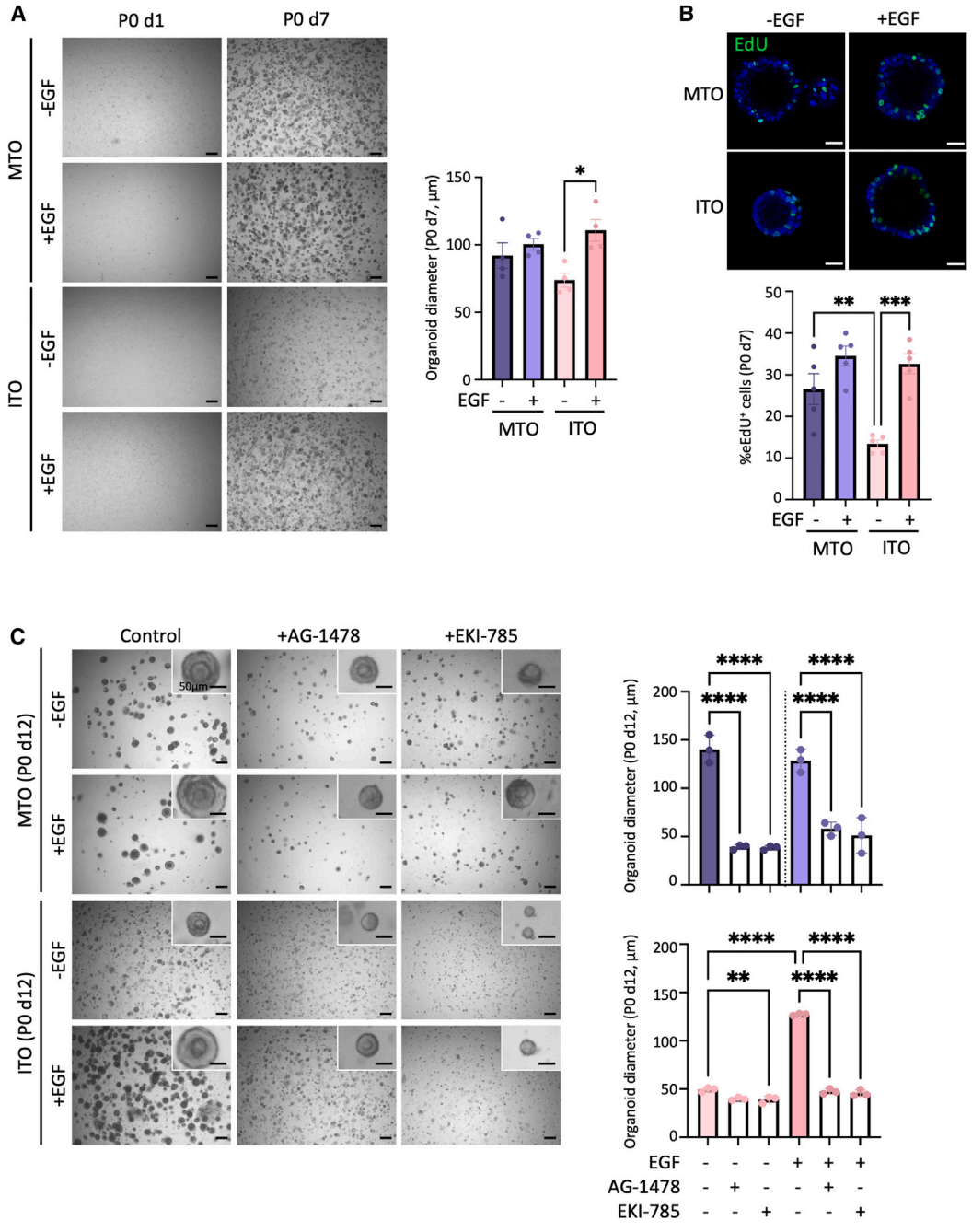

(legend on next page)

(Figure 2C). When EGF is added to ITOs that are first grown in TOM without EGF for 5 days, organoid growth (diameter) is increased (versus growth without EGF for the full period) (Figure S2D). When EGF is removed after the first 5 days in the presence of EGF, ITO growth is decreased (versus growth with EGF for the full period). In contrast, molar-derived organoids are insensitive to analogous removal or addition of exogenous EGF (Figure S2D). Thus, MTOs appear to have sufficient endogenous EGF(R) activity for optimal growth, whereas ITOs show better growth when the system is exogenously stimulated. In accordance, expression of several EGF family ligands that signal through the EGF receptor family (via homo- or heterodimerization of EGFR, ErbB2, ErbB3, and ErbB4), including *Areg*, *Btc*, *Hbegf*, *Epgn*, *Nrg2*, *Nrg3*, and *Nrg4*) (Wee and Wang, 2017), is higher in MTOs than ITOs (Figure 2D).

Taken together, MTOs and ITOs represent interesting tools to *in vitro* study tooth-specific molecular signaling and development. Due to better growth characteristics of ITOs in the presence of EGF (Figures 2A–2C, S2C, and S2D), we supplemented TOM with EGF for all further experiments in which MTOs and ITOs were compared.

MTOs and ITOs are amenable to AB-resembling differentiation

During tooth development, DESCs differentiate into ABs, which form the tooth enamel (Hermans et al., 2021) by first depositing EMP, to subsequently enable mineralization and formation of hydroxyapatite crystals using the deposited protein matrix as a guide (Bai et al., 2020; Welborn, 2020). During this process, differentiating DESCs first acquire a secretory-stage phenotype (sABs, which produce the EMP scaffold) and then a maturation-stage nature (mABs, which drive mineralization and degrade the EMP template), each characterized by distinct EMP profiles (AMELX/AMBN and ODAM/AMTN expression, respectively) (Ganss and Abbarin, 2014; Welborn, 2020). Here, we investigated whether the DESC organoids are able to differentiate toward ABs. Therefore, we removed stemness- and proliferation-promoting growth factors from TOM and added BMP2, BMP4, and TGFβ1 (Table S2; further referred to as differentiation medium [DM]), signaling factors that have been shown to be important for *in vivo* AB development (Gao et al., 2009; Xie et al., 2016).

Organoids (P5), expanded in TOM for 7 days, were switched to DM for an additional 7 days, causing no overt morphological changes (Figure 3A). However, interestingly, a prominent increase in EMP expression at protein (AMELX, ODAM) and/or gene (*Ambn*, *Amtn*, *Odam*) level was observed (Figures 3B and S3A). RNA-seq analysis revealed clear shifts in PCA pattern upon culture in DM, overall showing clustering of samples according to tooth type and culture condition (Figure S3B and supplemental information). Differentially expressed gene (DEG) analysis uncovered 400 upregulated genes in MTO+DM compared with MTO+TOM, and 1,357 upregulated genes in ITO+DM compared with ITO+TOM, of which 233 are shared between both organoid types (Figures 3C and S3C). Numerous amelogenesis-associated genes are found enriched in DM-exposed MTOs and ITOs versus TOM-grown controls, such as *Fam20a*, *Relt*, and *Wdr72*; the EMPs *Amtn* and *Odam*; and the matrix metallopeptidases *Mmp9* and *Mmp13* (Figure 3C) (El-Sayed et al., 2009; O'Sullivan et al., 2011; Feng et al., 2012; Kim et al., 2019; Vasconcelos et al., 2019). In addition, organoids exposed to DM express *Gm17660*, belonging to the same gene family and genomic locus as *Amtn* and *Odam*, and associated with mABs and the tooth epithelium-derived and enamel-bound junctional epithelium (JE) (Ganss and Abbarin, 2014; Moffatt et al., 2014; Yajima-Himuro et al., 2014). Gene ontology (GO) analysis further supported the acquisition of an AB-resembling fate in DM- versus TOM-grown organoids, identifying biological processes such as "amelogenesis" and "odontogenesis" (i.e., tooth development) as significantly enriched upon DM culture (Figure 3D). Simultaneously,

Figure 2. Differential response of TOs to exogenous EGF depending on tooth of origin

(A) *Left*: bright-field images of P0 d1 and d7 TOs grown in TOM without exogenous EGF (−EGF) or with EGF (+EGF). *Right*: bar graph (mean ± SEM) showing organoid diameter on d7. Data points represent biological replicates from independently established organoid lines; one-way analysis of variance (ANOVA) with Šídák's multiple comparisons test.

(B) *Top*: proliferative activity of TOs grown with or without EGF as assessed by EdU incorporation (green). Nuclei are counterstained with Hoechst33342 (blue). *Bottom*: bar graph showing the proportion of EdU^+ cells in TOs (mean ± SEM). Data points represent biological replicates from independently established organoid lines; one-way ANOVA with Šídák's multiple comparisons test.

(C) *Left*: bright-field images of P0 d12 TOs grown in TOM−EGF or TOM+EGF and treated with EGFR inhibitors AG-1478 or EKI-785. *Right*: bar graphs (mean ± SEM) showing TO diameter on d12. Data points represent biological replicates from independently established organoid lines; one-way ANOVA with Šídák's multiple comparisons test.

(D) Heatmap of gene expression of EGF pathway ligands in TOs (grown without EGF) as quantified by qRT-PCR analysis. Data are presented as relative expression to *Gapdh* (ΔC_t) and *Z* score normalized. Colors range from blue (low expression) to yellow (high expression).

Scale bars: 250 μm for bright-field images and 25 μm for IF images, unless indicated otherwise. *p < 0.05, **p < 0.01, ***p < 0.001, ****p < 0.0001. See also Figure S2.

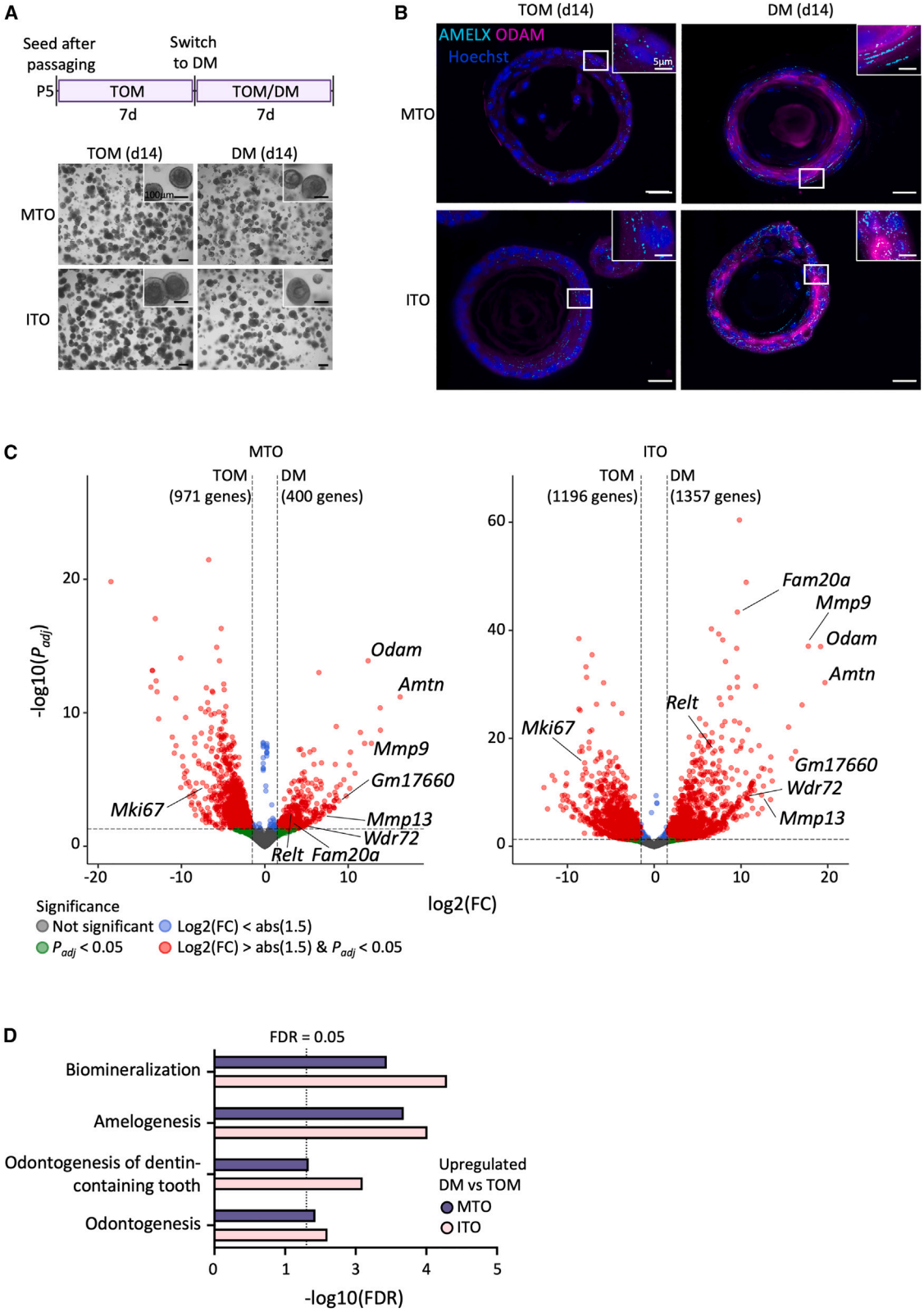

(legend on next page)

GO analysis revealed upregulation of apoptosis processes in DM-grown TOs (Figure S3D). Apoptosis is a natural step in the AB life cycle, with ABs undergoing apoptosis during the transition from sABs to mABs and in early mAB stage (Abramyan et al., 2021). Quantification of cleaved caspase-3 (CC3) immunofluorescence shows an increased number of apoptotic cells upon DM culture in both MTOs and ITOs (Figure S3E). Their proportion (20%–30%) is very similar to the reported proportion observed *in vivo* (25%) during both transition from sABs to mABs as well as in early mAB stage (Smith and Warshawsky, 1977). Simultaneously, the number of proliferating (Ki67$^+$) cells goes down (Figure S3F), further corroborated by decreased *Mki67* expression (Figure 3C) and downregulated "cell cycle" processes in DM- versus TOM-cultured TOs (Figure S3G).

Together, our findings indicate that our organoid models, both from molar and incisor, are amenable to differentiation toward AB-resembling cells *in vitro*. From the data obtained, it appears that the acquired phenotype more resembles the mAB than the preceding sAB stage, as supported by predominant increase of mAB markers and noticeable apoptosis.

Assembloids combining organoid DESCs with mesenchymal dental pulp stem cells recapitulate developmental epithelial-mesenchymal interactions and co-differentiation

During tooth development, the DE generates ABs while the dental mesenchyme contributes to the dentin-producing odontoblasts (OBs) and root cement-fabricating cementoblasts (CBs) (Hermans et al., 2021). Throughout the various stages of tooth development, epithelial-mesenchymal interactions play a crucial role, driving odontogenesis and differentiation of the mature cell types (Hermans et al., 2021). To mimic these developmental interactions, we established a co-culture model by combining TO DESCs with mesenchymal dental pulp stem cells (DPSCs), following a similar approach as we previously described for human tooth (Figure 4A; see experimental procedures) (Hemeryck et al., 2022). These tooth "assembloids" (referring to self-organizing 3D cellular constructs resulting from the combination of epithelial organoids with other cell types such as mesenchymal cells; Rawlings et al., 2021; Kanton and Paşca, 2022) were established and cultured either in a 1:1 ratio of TOM and pulp medium (PM) or a 1:1 ratio of DM and pulp differentiation medium (PDM) (Figure 4A; Tables S3 and S4). The molar and incisor assembloids (referred to as MAs and IAs, respectively) show similar morphology that changes according to culture medium (Figure 4B). TOM/PM-grown assembloids mainly display a bubbled outline composed of small organoid units, whereas DM/PDM-grown assembloids largely show a smooth contour. In all conditions, the assembloids contain distinct epithelial (CK14$^+$) and mesenchymal (vimentin, VIM$^+$) domains (Figure 4B).

To more granularly characterize the tooth assembloids, we applied scRNA-seq analysis on MAs and IAs grown in TOM/PM and DM/PDM conditions (Table S5). Following quality control, data processing, and integration, 43,891 cells were retained (Figures S4A and S4B). Eleven distinct clusters were discerned and annotated, based on marker expression (Figures 4C, 4D, S4C, and S4D) (Hermans et al., 2022). As expected, two large "superclusters" of epithelial or mesenchymal cells were identified. Within the epithelial supercluster, several clusters were classified including "cycling" cells, non-cycling non-differentiated "epithelial" cells, progenitor cells ("Prog" #1, #2, and #3), and two distinct, more differentiated cell populations, i.e., a "mAB-like" (*Amtn*$^+$/*Odam*$^+$/*Mmp9*$^+$/*Gm17660*$^+$) and "JE-like" (*Ly6D*$^+$/*Il1rn*$^+$/*BC037156*$^+$ [also known as *Fdcsp*]) cell cluster, both more abundant in DM/PDM-grown assembloids (Figures 4C, 4D, S4C, and S4D) (Feng et al., 2012; Ganss and Abbarin, 2014; Hermans et al., 2022). Comparison of the top 20 DEGs between mAB- and JE-like clusters further confirmed specific expression of amelogenesis-associated genes (*Amtn*, *Odam*, *Mmp9*, *Gm17660*, *Lamc2*, *Lama3*, *Lamb3*, and *Tmsb4x*) or JE-linked genes (*Ly6d*, *Il1rn*, *BC037156* [*Fdcsp*], and *Anxa1*) in the respective clusters (Figure S4D) (Hayashi et al., 2010; Feng et al., 2012; Kim et al., 2013; Ganss and Abbarin, 2014; Kiyoshima et al., 2014; Moffatt et al., 2014; Gostyńska et al., 2016; Wazen et al., 2016; Hermans et al., 2022). Both groups of genes were elevated in DM/PDM-cultured compared with TOM/PM-grown assembloids, indicating

Figure 3. *In vitro* differentiation of TOs toward AB-resembling cells

(A) *Top*: timeline of experimental setup. *Bottom*: bright-field images of P5 d14 TOs grown in TOM or switched to DM after 7 days. Magnified view is in boxes.

(B) IF analysis of AMELX (cyan) and ODAM (magenta) in TOs. Nuclei are counterstained with Hoechst33342 (blue). Boxed areas are magnified.

(C) Volcano plot with $\log_2$(fold change [FC]) versus –log10(P_{adj}) value) of RNA-seq data from MTOs (left panel) and ITOs (right panel). Statistically upregulated genes between TOM- and DM-grown TOs (left for TOM and right for DM) are indicated in red, as determined by a combination of $\log_2$(FC) > the absolute (abs) value of ±1.5 and $P_{adj} < 0.05$.

(D) Significant (FDR $\leq$ 0.05, indicated by dotted line) DEG-based GO terms enriched in DM-grown TOs compared with TOM-cultured controls. Scale bars: 250 μm for bright-field images and 25 μm for IF images, unless indicated otherwise. See also Figure S3.

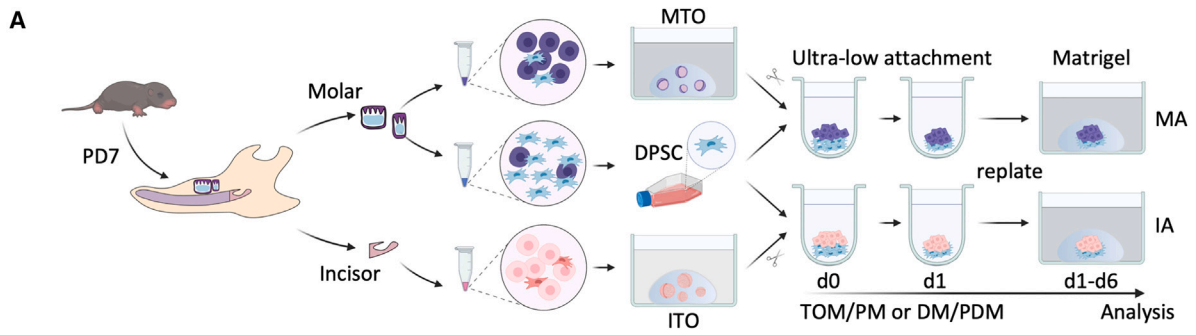

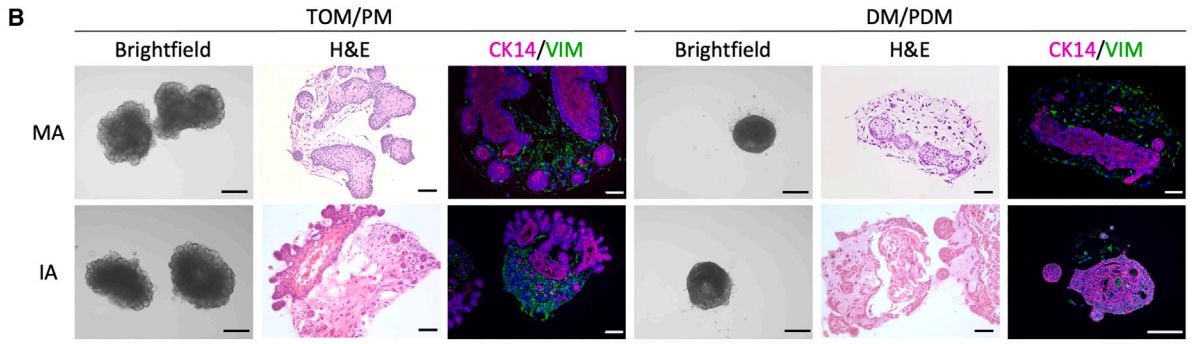

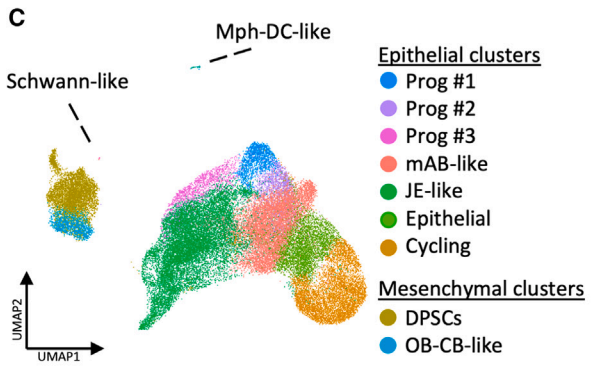

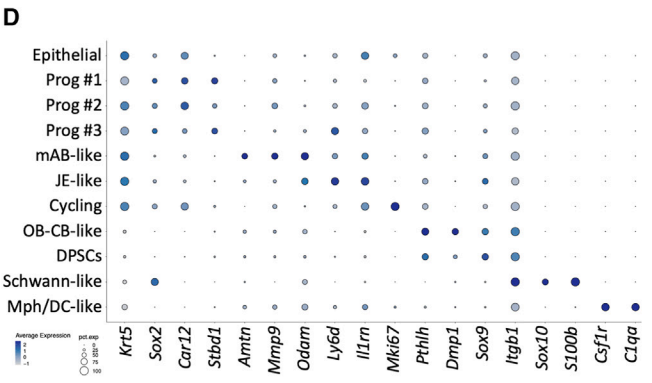

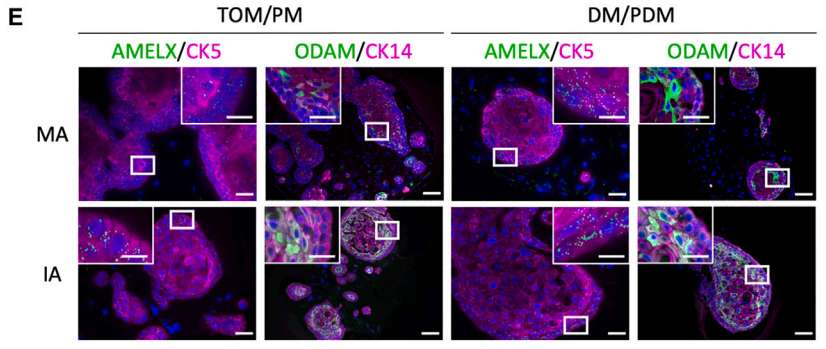

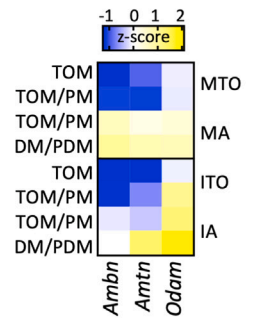

(legend on next page)

enhanced differentiation and maturation when exposed to differentiation media (Figure S4E). Expression of JE-related genes is also detected in the monocultured MTOs and ITOs and found upregulated following culture in DM (Figures S4F and S4G), indicating that mesenchymal interaction is not essentially needed for the acquisition of a JE-like cell fate. On the other hand, assembloids show enhanced differentiation toward AB-resembling cells compared with organoid monocultures, which is still further promoted by exposure to DM/PDM (Figures 4E, 4F, S4C–S4E). Indeed, whereas TOM-cultured TOs lack ODAM expression and TOM/PM-cultured organoids show no or only little ODAM protein signal (Figure S4H), the presence of DPSCs is sufficient to lead to prominent ODAM signal in the assembloid epithelium, which is visibly further enhanced by exposure to DM/PDM (Figure 4E). Similarly, gene expression of *Ambn*, *Amtn*, and *Odam* is augmented in assembloids compared with TOs alone, and further elevated when cultured in DM/PDM (Figure 4F).

Regarding the mesenchymal supercluster, both DPSCs and OB-CB-like cells (*Dmp1*$^{+}$/*Pthlh*$^{+}$) are discerned (Figures 4C and 4D). Gene expression analysis of known OBs (*Dspp*, *Dmp1*), CBs (*Pthlh*), and mineralization markers (*Ibsp, Spp1*, and *Col1a1*) shows upregulation in DM/PDM culture, thereby supporting their further differentiation (Figures 4C, 4D, and S4I). Unexpectedly, a small cluster of "Schwann-like" cells (*Sox10*$^{+}$/*S100b*$^{+}$) is identified in DM/PDM-grown assembloids (Figures 4C, 4D, and S4C). In previous work, we have shown that human DPSCs can differentiate into Schwann cells *in vitro* (Martens et al., 2014), although not yet demonstrated for mouse DPSCs. Finally, a small cluster of macrophage/dendritic cell-like ("Mph-DC-like") cells (*Csf1r*$^{+}$/*C1qa*$^{+}$) of unknown origin is detected in the assembloids, more clearly after culture in DM/PDM (Figures 4C, 4D, and S4C).

Taken together, combining organoid DESCs with mesenchymal DPSCs empowers the differentiation toward (m) AB-resembling as well as OB-CB-like cells, thereby mimicking the key outcome of developmental epithelial-mesenchymal interactions as occurring *in vivo*. Interestingly, acquisition of a JE-like fate was also observed. During tooth development, the JE is derived from the DE, likely from both the "reduced enamel epithelium" (REE; i.e., the layer of mAB and outer enamel epithelium covering the deposited enamel prior to eruption) and the DESC-containing epithelial cell rests of Malassez (ERM) (Kato et al., 2019; Hermans et al., 2022). Together, our findings propose that the organoids/assembloids acquire a late-stage DE phenotype, encompassing both mAB and JE phases.

In vivo survival and differentiation potential of mouse TOs

To evaluate whether mouse TOs are able to survive and differentiate *in vivo*—a requirement for future tooth regeneration/replacement endeavors—we applied TOM-grown ITOs in two complementary *in vivo* transplantation assays, i.e., subcutaneous (s.c.) implantation into immunodeficient (nude) mouse of a 3D printed hydroxyapatite scaffold seeded with Matrigel and organoids (Hemeryck et al., 2022) or grafting onto chicken chorioallantoic membrane (CAM) (Bronckaers et al., 2013, 2021) (Figure 5A). In both models, ITOs are able to survive, retain epithelial nature (CK14^{+}), and produce both AMELX and ODAM (Figures 5B and 5C) (the latter not present before transplantation, see, e.g., Figure 3B). Together, these proof-of-principle experiments show that mouse TOs are able to survive and spontaneously differentiate toward AB-like cells *in vivo*.

DISCUSSION

In this study, we report the development of long-term expandable TOs from mouse molar and incisor. The established TOs recapitulate key properties of mouse DE. In contrast to many other available methods to study DE

Figure 4. Establishment and characterization of tooth assembloids combining organoid DESCs with mesenchymal DPSCs

(A) Schematic of experimental setup for the development of tooth assembloids by combining TO cells with mesenchymal DPSCs.

(B) Bright-field, H&E, and IF (of indicated markers) images of MAs and IAs grown in TOM/PM or DM/PDM. Nuclei of IF images are counterstained with Hoechst33342.

(C) Annotated UMAP plot of integrated assembloid scRNA-seq datasets, i.e., from MA+TOM/PM, MA+DM/PDM, IA+TOM/PM, and IA+DM/PDM (n = 2 biological replicates of each experimental condition).

(D) Dotplot displaying the percentage of cells (dot size) expressing key marker genes of the different annotated cell clusters (average expression levels indicated by color intensity; see scale).

(E) IF analysis of AMELX and ODAM (green) and indicated cytokeratins (CK; magenta) in tooth assembloids. Nuclei are counterstained with Hoechst33342 (blue). Boxed areas are magnified.

(F) Heatmap of gene expression of AB-resembling differentiation in tooth assembloids as quantified by qRT-PCR analysis. Data are presented as relative expression to *Gapdh* (ΔC_t) and *Z* score normalized. Colors range from blue (low expression) to yellow (high expression).

Scale bars: 250 μm for bright-field images, 50 μm for H&E, CK14/VIM, and ODAM/CK14 (20 μm for close-ups) IF images, 25 μm for AMELX/CK5 (10 μm for close-ups) IF images. See also Figure S4.

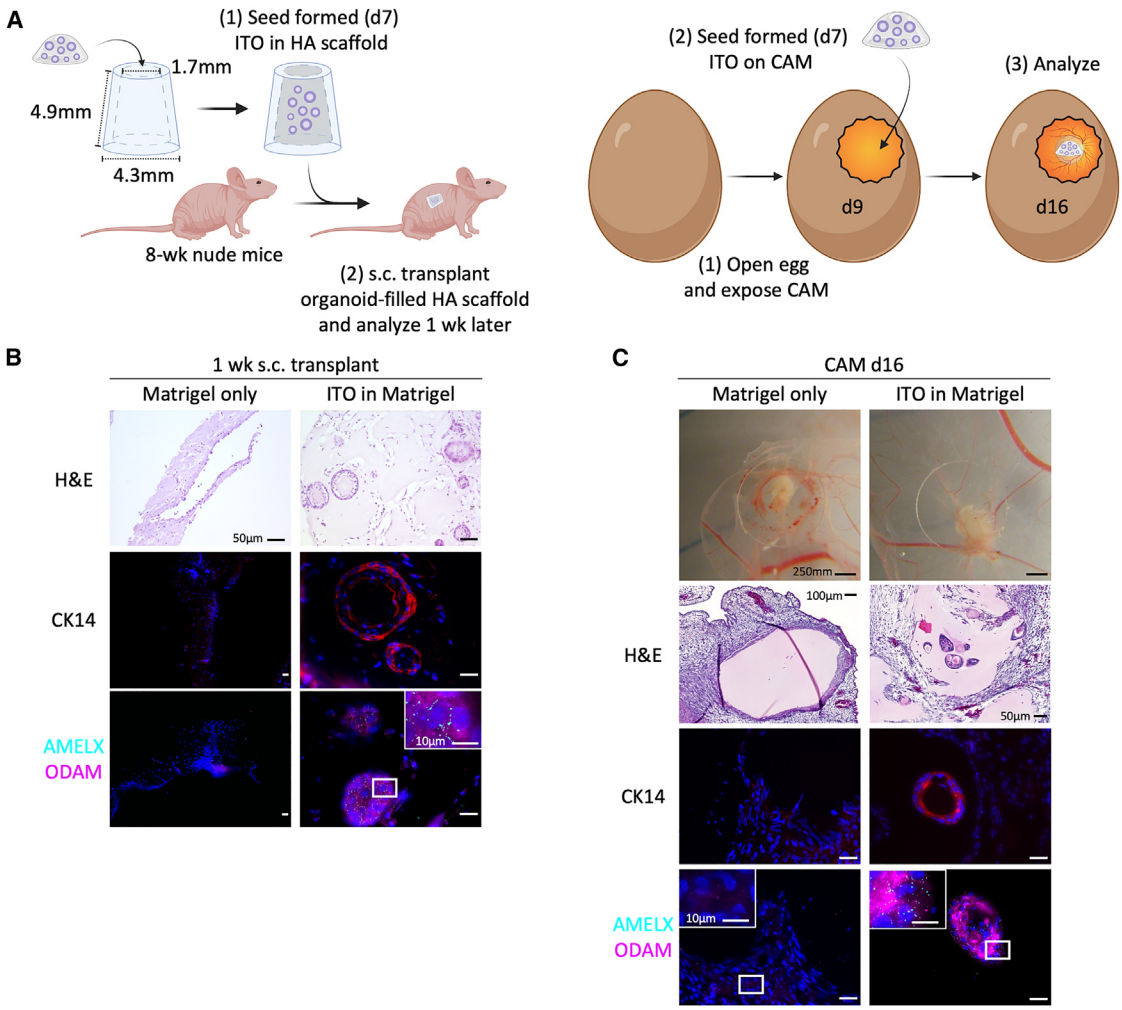

Figure 5. *In vivo* survival and differentiation potential of TOs

(A) Schematic overview of *in vivo* transplantation approaches. *Left*: s.c. transplantation of ITOs seeded in 3D-printed hydroxyapatite (HA) construct. *Right*: grafting onto chicken CAM.

(B) H&E and IF (of indicated markers) images of s.c. transplanted ITOs or negative controls (Matrigel only) after 1 week (wk).

(C) CAM, H&E, or IF (of indicated markers) images of grafted ITOs or negative controls (Matrigel only) at d10. Boxed areas are magnified. Scalebars: 50 μm for H&E, 25 μm for IF, and 250 mm for CAM images, unless otherwise indicated.

in vitro, our TO model provides more accurate mirroring of tooth-specific biology *in vitro*. Among others, our observations support a previous study in which ISL1 was abundantly detected in developing mouse incisors but only barely in emerging molars (Naveau et al., 2017). Moreover, genetic deletion of *Isl1* in the DE resulted in incisor but not molar enamel defects (Naveau et al., 2017). In addition to displaying tooth-specific expression profiles, both MTOs and ITOs show tooth-specific responses to exogenous growth factor signaling as shown by differential response to EGF supplementation, which, importantly, recapitulates *in vivo* observations. Indeed, perinatal injection of EGF in rodents results in precocious eruption of incisors but not rodents (Rhodes et al., 1987; Cielinski et al., 1995; Naveau et al., 2017). Current models are either developed from one tooth type (i.e., immortalized cell lines derived from molar enamel organ) or are not specified (i.e., differentiation of AB/DE-like cells from 2D pluripotent stem cells), whereas other methods are not expandable and start from embryonic material (Nakao et al., 2007; Sarkar et al., 2014; Miao et al., 2021). The ability to mimic tooth-type-specific paradigms and development *in vitro* will be invaluable to further elucidate key factors and pathways driving differential development of both tooth types.

In addition, we show that both MTOs and ITOs are amenable to *in vitro* differentiate toward AB-like cells,

either alone or when activated by co-culture with DPSCs, mirroring signaling interactions naturally occurring *in vivo*. Notably, our data suggest that AB differentiation appears predisposed toward a more mature phenotype, representing the mAB stage, which *in vivo* plays an important role in the final mineralization and maturation of the tooth enamel. Firstly, DM-grown TOs and assembloids predominantly express the mAB EMP markers *Amtn* and *Odam*/ODAM, as well as other mAB markers such as *Gm17660* (Ganss and Abbarin, 2014). Secondly, differentiation of TOs is accompanied by a loss of proliferation and increased apoptosis. The latter phenomenon is strongly associated with the transition from sAB to the mAB stage, as well as during the early mAB stage of the AB life cycle (Smith and Warshawsky, 1977). Interestingly, the proportion of apoptotic cells in DM-grown organoids was similar to the proportion identified *in vivo* (Smith and Warshawsky, 1977).

At the same time, our data suggest the acquisition of a JE-like cell fate in DM-grown TOs and in assembloids. *In vivo*, JE plays an important role forming the bridge between the enamel surface and oral gingival epithelium, and it functions as an important immunological barrier to oral micro-organisms (Fischer and Aparicio, 2022). Previously, use of bioengineered tooth germs revealed that the JE is derived from the odontogenic DE, which also gives rise to the AB lineage (Yajima-Himuro et al., 2014). Although JE is traditionally thought to develop from the REE (and thus from mABs and outer enamel epithelium), there is previously reported support that ERM may also contribute to JE (Kato et al., 2019; Hermans et al., 2022). Further analysis of TOs and assembloids (including our developed ERM-derived human tooth models; Hemeryck et al., 2022) during differentiation (i.e., at different timepoints) may provide further insight into these hypotheses. Together, the presence of both mAB- and JE-like cells suggests that our currently developed differentiation protocols drive TOs toward a more mature, late-stage DE phenotype. Further development and optimization of differentiation protocols to specifically enrich for one specific cell type (i.e., mAB- or JE-like cells) or to instead acquire sAB nature will provide a tunable and flexible model for future research.

Importantly, organoids are highly adaptable tools for disease modeling and regenerative medicine or tooth bioengineering endeavors. TOs can be derived from transgenic mouse models of tooth disease (e.g., mice mimicking amelogenesis imperfecta), thereby having the ethical advantage of reducing the number of animals used, as organoids are highly amendable (Gibson et al., 2001; Paine et al., 2003; Pugach and Gibson, 2014). Another application may be co-culture with oral micro-organisms to study the immunological barrier function of JE. In addition, due to their high, long-term expandability *in vitro* and ability to survive and differentiate *in vitro* and *in vivo* (as demonstrated in this study), TOs are an ideal cellular source of DE cells for tooth tissue bioengineering. Finally, through enabling epithelial-mesenchymal reciprocal signaling, epithelial TOs may be the missing link needed to stimulate *in vitro* differentiation of OBs. Considerable research has established that DPSCs can differentiate into mineralizing cells resembling OBs; however, an accurate representation of OBs is still lacking (Tsutsui, 2020). Data from our developed tooth assembloids indicate that DPSCs may acquire an OB-CB-like phenotype. Further research is now needed to optimize the differentiation parameters for development of authentic OBs *in vitro*.

In summary, this novel mouse TO model provides a valuable tool to study mouse tooth DE/DESCs, dental epithelial-mesenchymal interactions, and AB/JE differentiation while allowing further elucidation of tooth-type-specific features. As such, TOs, both from mouse molar and incisor as developed here and from human ERM obtained from extracted third molars as previously described (Hemeryck et al., 2022), have great potential to further unravel tooth biology and repair and may be an alluring tool to eventually enable tooth bioengineering strategies.

EXPERIMENTAL PROCEDURES

Detailed methods are provided in the supplemental information.

Resource availability

Corresponding author

Further information and requests for resources and reagents should be directed to and will be fulfilled upon reasonable request by the corresponding authors, Annelies Bronckaers (annelies.bronckaers@uhasselt.be) and Hugo Vankelecom (hugo.vankelecom@kuleuven.be).

Materials availability

The study did not generate new unique reagents.

Data availability

RNA-seq and scRNA-seq data have been deposited to the ArrayExpress database (accession numbers E-MTAB-12557 [https://www.ebi.ac.uk/biostudies/arrayexpress/studies/E-MTAB-12557?accession=E-MTAB-12557] and E-MTAB-12544 [https://www.ebi.ac.uk/biostudies/arrayexpress/studies/E-MTAB-12544?accession=E-MTAB-12544]).

Establishing organoid cultures from mouse molar and incisor

Whole (unerupted) molars, including surrounding dental follicle and attached epithelium, as well as apical ends of (unerupted) incisors were carefully isolated from PD7 mice (ethical approval P056/2022, KU Leuven). Dissociated molar and incisor DE cell material was plated in serum-free defined medium (SFDM; Table S1) and growth factor-reduced Matrigel at a 30:70 ratio and cultured in defined TOM (Table 1). TOs were passaged every 7–10 days.

Establishment of mouse tooth assembloids

Mouse tooth assembloids were established using a similar protocol as we previously described for human tooth assembloids (Hemeryck et al., 2022). Briefly, single-cell dissociated TOs and DPSCs were combined in round-bottom low-attachment plates using a layered approach and cultured in 10% growth factor reduced Matrigel with 90% of either a 1:1 mixture of TOM/PM or DM/PDM. After 24 h, the formed structures were plated in 70% Matrigel to generate tooth assembloids that were maintained in the respective 1:1 media mixtures.

Histochemical, immunostaining, EdU incorporation, and TEM analysis

Samples were fixed in paraformaldehyde and paraffin embedded. Derived sections were subjected to hematoxylin and eosin (H&E) or immunofluorescence staining (for antibodies, see Table S6). EdU labeling in TOs was performed using the Click-iT EdU Alexa Fluor 488 kit (Thermo Fisher Scientific) according to the manufacturer's instructions. TO samples were prepared for TEM as previously described in detail (Lambrichts et al., 1993; Cox et al., 2019). For all analyses, representative images are shown.

Gene expression analysis by qRT-PCR

Total RNA from dissociated molar and incisor tissue, TOs, and tooth assembloids was subjected to quantitative reverse transcription (real-time) PCR (qRT-PCR) using specific forward and reverse primers (Table S7), all as described before (Cox et al., 2019). Gene expression levels were calculated as ΔCt values relative to *Gapdh* ($Ct_{target} - Ct_{housekeeping}$), and *Z* score normalization was performed.

RNA-seq analysis

For bulk RNA-seq analysis, RNA was isolated from P0 MTOs and ITOs grown in TOM or from P5 MTOs and ITOs grown in TOM+EGF and exposed to DM or not. For scRNA-seq analysis, MAs and IAs, exposed to DM/PDM or not, were dissociated into single cells.

Subcutaneous transplantation of ITOs

Matrigel with d7 ITOs (P5) was pipetted into hydroxyapatite scaffolds that were s.c. grown in immunodeficient mice for 1 week, as in detail described elsewhere (Bronckaers et al., 2021; Hemeryck et al., 2022) (ethical approval protocol 202138, UHasselt).

Chicken CAM assay

CAM assay was performed as previously in detail described (Bronckaers et al., 2013). In short, pre-solidified Matrigel droplets with d7 ITOs (P5) were applied onto the CAM of fertilized eggs, and the graft was removed 1 week later. Droplets of Matrigel alone served as negative controls.

Statistical analysis

Statistical analyses were performed using GraphPad Prism (v9.3.1) for macOS and are specified in the figure legends. All experiments were performed with ≥ 3 (unless otherwise indicated) independent biological experiments (i.e., organoid lines established from independent mouse litters).

SUPPLEMENTAL INFORMATION

Supplemental information can be found online at https://doi.org/10.1016/j.stemcr.2023.03.011.

AUTHOR CONTRIBUTIONS

F.H. designed the concepts and experiments, performed the experiments and the data analysis, interpreted the results, and wrote the manuscript. L.H. co-designed the concepts and provided technical and conceptual input. C.B. contributed to organoid differentiation experiments. M.T.P. contributed to assembloid experiments. S.H. contributed to TEM analysis. H.K. performed and co-interpreted TEM analysis. D.L. co-supervised the scRNA-seq experiments. I.L. co-supervised the project, co-designed concepts and experiments, and co-interpreted results. A.B. co-supervised the project, co-designed concepts and experiments, performed TEM and *in vivo* experiments, co-interpreted the results and co-wrote the manuscript. H.V. supervised the entire project, co-designed the organoid concepts and experiments, co-interpreted the results, and vastly amended the manuscript. All co-authors critically read and approved the manuscript.

ACKNOWLEDGMENTS

We are grateful to Evelyne Van Kerckhove (UHasselt), Marc Jans (UHasselt), Jeanine Santermans (UHasselt), and Veerle Vanslembrouck (KU Leuven) for valuable technical help. We thank Dr. Diether Lambrechts' group (VIB, KU Leuven) for technical assistance in 10× Genomics. Computational resources for transcriptome analyses were provided by the "Vlaams Supercomputer Centrum" (VSC), managed by the Fund for Scientific Research (FWO), Flanders (Belgium). We are also grateful to the Imaging Core (VIB, KU Leuven) and the CIC (KU Leuven) for use of microscopes and the Center for Brain & Disease Research (CBD) Histology unit (VIB, KU Leuven) for use of histology equipment. We acknowledge the use of the TEM platforms at VIB-KU Leuven, UHasselt, and Tohoku University. The authors also thank Dr. Adrian Ranga (KU Leuven), Dr. Ronald Driesen (UHasselt), and other non-coauthor members of the Laboratory of Tissue Plasticity in Health and Disease (KU Leuven) for their input. Certain figures were created using BioRender.com or GraphPad Prism (v9.3.1) for macOS.

This work was supported by grants from KU Leuven (Research Fund) and Fund for Scientific Research (FWO) Flanders. L.H. was an FWO PhD Fellow (1S84718N). C.B. is an FWO PhD Fellow (1129323N), while F.H. was supported by an FWO project grant (G061819FWO). Use of the Zeiss LSM 780 – SP Mai Tai HP DS is supported by Hercules AKUL/11/37 and FWO G.0929.15 funding to Dr. Pieter Vanden Berghe (CIC, KU Leuven), while the application of the JEOL FLASH 1400 TEM was supported by Hercules FWO funding I000220N to I.L.

CONFLICT OF INTERESTS

The authors declare no competing interests.

Received: January 31, 2023
Revised: March 22, 2023
Accepted: March 23, 2023
Published: April 20, 2023

REFERENCES

Abramyan, J., Geetha-Loganathan, P., Šulcová, M., and Buchtová, M. (2021). Role of cell death in cellular processes during odontogenesis. Front. Cell Dev. Biol. *9*, 671475. https://doi.org/10.3389/fcell.2021.671475.

Artegiani, B., and Clevers, H. (2018). Use and application of 3D-organoid technology. Hum. Mol. Genet. *27*, R99–R107. https://doi.org/10.3389/fcell.2021.671475.

Bai, Y., Yu, Z., Ackerman, L., Zhang, Y., Bonde, J., Li, W., Cheng, Y., and Habelitz, S. (2020). Protein nanoribbons template enamel mineralization. Proc. Natl. Acad. Sci. USA *117*, 19201–19208. https://doi.org/10.1073/pnas.2007838117.

Binder, M., Biggs, L.C., Kronenberg, M.S., Schneider, P., Thesleff, I., and Balic, A. (2020). Novel strategies for expansion of tooth epithelial stem cells and ameloblast generation. Sci. Rep. *10*, 4963. https://doi.org/10.1038/s41598-020-60708-w.

Boretto, M., Cox, B., Noben, M., Hendriks, N., Fassbender, A., Roose, H., Amant, F., Timmerman, D., Tomassetti, C., Vanhie, A., et al. (2017). Development of organoids from mouse and human endometrium showing endometrial epithelium physiology and long-term expandability. Development *144*, 1775–1786. https://doi.org/10.1242/dev.148478.

Bronckaers, A., Hilkens, P., Fanton, Y., Struys, T., Gervois, P., Politis, C., Martens, W., and Lambrichts, I. (2013). Angiogenic properties of human dental pulp stem cells. PLoS One *8*, e71104. https://doi.org/10.1371/journal.pone.0071104.

Bronckaers, A., Hilkens, P., Wolfs, E., and Lambrichts, I. (2021). By the skin of your teeth: a subcutaneous mouse model to study pulp regeneration. In Vascular Morphogenesis. Methods in Molecular Biology, D. Ribatti, ed. (Humana Press Inc.), pp. 223–232. https://doi.org/10.1007/978-1-0716-0916-3_16.

Catón, J., Luder, H.U., Zoupa, M., Bradman, M., Bluteau, G., Tucker, A.S., Klein, O., and Mitsiadis, T.A. (2009). Enamel-free teeth: Tbx1 deletion affects amelogenesis in rodent incisors. Dev. Biol. *328*, 493–505. https://doi.org/10.1016/j.ydbio.2009.02.014.

Cielinski, M.J., Jolie, M., Wise, G.E., and Marks, S.C. (1995). The contrasting effects of colony-stimulating factor-1 and epidermal growth factor on tooth eruption in the rat. Connect. Tissue Res. *32*, 165–169. https://doi.org/10.3109/03008209509013720.

Clevers, H. (2016). Modeling development and disease with organoids. Cell *165*, 1586–1597. https://doi.org/10.1016/j.cell.2016.05.082.

Cox, B., Laporte, E., Vennekens, A., Kobayashi, H., Nys, C., Van Zundert, I., Uji-I, H., Vercauteren Drubbel, A., Beck, B., Roose, H., et al. (2019). Organoids from pituitary as a novel research model toward pituitary stem cell exploration. J. Endocrinol. *240*, 287–308. https://doi.org/10.1530/JOE-18-0462.

El-Sayed, W., Parry, D.A., Shore, R.C., Ahmed, M., Jafri, H., Rashid, Y., Al-Bahlani, S., Al Harasi, S., Kirkham, J., Inglehearn, C.F., and Mighell, A.J. (2009). Mutations in the beta propeller WDR72 cause autosomal-recessive hypomaturation amelogenesis imperfecta. Am. J. Hum. Genet. *85*, 699–705. https://doi.org/10.1016/j.ajhg.2009.09.014.

Feng, J., McDaniel, J.S., Chuang, H.H., Huang, O., Rakian, A., Xu, X., Steffensen, B., Donly, K.J., MacDougall, M., and Chen, S. (2012). Binding of amelogenin to MMP-9 and their co-expression in developing mouse teeth. J. Mol. Histol. *43*, 473–485. https://doi.org/10.1007/s10735-012-9423-1.

Fischer, N.G., and Aparicio, C. (2022). Junctional epithelium and hemidesmosomes: tape and rivets for solving the "percutaneous device dilemma" in dental and other permanent implants. Bioact. Mater. *18*, 178–198. https://doi.org/10.1016/j.bioactmat.2022.03.019.

Fujii, M., and Sato, T. (2020). Somatic cell-derived organoids as prototypes of human epithelial tissues and diseases. Nat. Mater. *20*, 156–169. https://doi.org/10.1038/s41563-020-0754-0.

Ganss, B., and Abbarin, N. (2014). Maturation and beyond: proteins in the developmental continuum from enamel epithelium to junctional epithelium. Front. Physiol. *5*, 371. https://doi.org/10.3389/fphys.2014.00371.

Gao, Y., Li, D., Han, T., Sun, Y., and Zhang, J. (2009). TGF-beta1 and TGFBR1 are expressed in ameloblasts and promote MMP20 expression. Anat. Rec. *292*, 885–890. https://doi.org/10.1002/ar.20901.

Gibson, C.W., Yuan, Z.A., Hall, B., Longenecker, G., Chen, E., Thyagarajan, T., Sreenath, T., Wright, J.T., Decker, S., Piddington, R., et al. (2001). Amelogenin-deficient mice display an amelogenesis imperfecta phenotype. J. Biol. Chem. *276*, 31871–31875. https://doi.org/10.1074/jbc.M104624200.

Gostyńska, K.B., Yan Yuen, W., Pasmooij, A.M.G., Stellingsma, C., Pas, H.H., Lemmink, H., and Jonkman, M.F. (2016). Carriers with functional null mutations in LAMA3 have localized enamel abnormalities due to haploinsufficiency. Eur. J. Hum. Genet. *25*, 94–99. https://doi.org/10.1038/ejhg.2016.136.

Hayashi, Y., Matsunaga, T., Yamamoto, G., Nishii, K., Usui, M., Yamamoto, M., and Tachikawa, T. (2010). Comprehensive analysis of gene expression in the junctional epithelium by laser microdissection and microarray analysis. J. Periodontal. Res. *45*, 618–625. https://doi.org/10.1111/j.1600-0765.2010.01276.x.

Hemeryck, L., Hermans, F., Chappell, J., Kobayashi, H., Lambrechts, D., Lambrichts, I., Bronckaers, A., and Vankelecom, H. (2022). Organoids from human tooth showing epithelial stemness phenotype and differentiation potential. Cell. Mol. Life Sci. *79*, 153. https://doi.org/10.1007/s00018-022-04183-8.

Hermans, F., Bueds, C., Hemeryck, L., Lambrichts, I., Bronckaers, A., and Vankelecom, H. (2022). Establishment of inclusive single-cell transcriptome atlases from mouse and human tooth as powerful resource for dental research. Front. Cell Dev. Biol. *10*, 1021459. https://doi.org/10.3389/fcell.2022.1021459.

Hermans, F., Hemeryck, L., Lambrichts, I., Bronckaers, A., and Vankelecom, H. (2021). Intertwined signaling pathways governing tooth development: a give-and-take between canonical wnt and shh. Front. Cell Dev. Biol. *9*, 758203. https://doi.org/10.3389/fcell.2021.758203.

Kanton, S., and Paşca, S.P. (2022). Human assembloids. Development *149*, dev201120. https://doi.org/10.1242/dev.201120.

Kato, M., Tanaka, J., Aizawa, R., Yajima-Himuro, S., Seki, T., Tanaka, K., Yamada, A., Ogawa, M., Kamijo, R., Tsuji, T., et al. (2019).

Visualization of junctional epithelial cell replacement by oral gingival epithelial cells over a life time and after gingivectomy. Sci. Rep. *9*, 7640. https://doi.org/10.1038/s41598-019-44065-x.

Kim, J.W., Seymen, F., Lee, K.E., Ko, J., Yildirim, M., Tuna, E.B., Gencay, K., Shin, T.J., Kyun, H.K., Simmer, J.P., and Hu, J.C.C. (2013). LAMB3 mutations causing autosomal-dominant amelogenesis imperfecta. J. Dent. Res. *92*, 899–904. https://doi.org/10.1177/0022034513502054.

Kim, J.W., Zhang, H., Seymen, F., Koruyucu, M., Hu, Y., Kang, J., Kim, Y.J., Ikeda, A., Kasimoglu, Y., Bayram, M., et al. (2019). Mutations in RELT cause autosomal recessive amelogenesis imperfecta. Clin. Genet. *95*, 375–383. https://doi.org/10.1111/cge.13487.

Kiyoshima, T., Fujiwara, H., Nagata, K., Wada, H., Ookuma, Y.F., Shiotsuka, M., Kihara, M., Hasegawa, K., Someya, H., and Sakai, H. (2014). Induction of dental epithelial cell differentiation marker gene expression in non-odontogenic human keratinocytes by transfection with thymosin beta 4. Stem Cell Res. *12*, 309–322. https://doi.org/10.1016/j.scr.2013.11.006.

Lambrichts, I., Creemers, J., and Van Steenberghe, D. (1993). Periodontal neural endings intimately relate to epithelial rests of Malassez in humans. A light and electron microscope study. J. Anat. *182*, 153–162.

Martens, W., Sanen, K., Georgiou, M., Struys, T., Bronckaers, A., Ameloot, M., Phillips, J., and Lambrichts, I. (2014). Human dental pulp stem cells can differentiate into Schwann cells and promote and guide neurite outgrowth in an aligned tissue-engineered collagen construct in vitro. Faseb. J. *28*, 1634–1643. https://doi.org/10.1096/fj.13-243980.

Miao, X., Niibe, K., Fu, Y., Zhang, M., Nattasit, P., Ohori-Morita, Y., Nakamura, T., Jiang, X., and Egusa, H. (2022). Epiprofin transcriptional activation promotes ameloblast induction from mouse induced pluripotent stem cells via the BMP-smad signaling Axis. Front. Bioeng. Biotechnol. *10*, 890882. https://doi.org/10.3389/fbioe.2022.890882.

Miao, X., Niibe, K., Zhang, M., Liu, Z., Nattasit, P., Ohori-Morita, Y., Nakamura, T., Jiang, X., and Egusa, H. (2021). Stage-specific role of amelx activation in stepwise ameloblast induction from mouse induced pluripotent stem cells. Int. J. Mol. Sci. *22*, 7195. https://doi.org/10.3390/ijms22137195.

Moffatt, P., Wazen, R.M., Dos Santos Neves, J., and Nanci, A. (2014). Characterisation of secretory calcium-binding phosphoprotein-proline-glutamine-rich 1: a novel basal lamina component expressed at cell-tooth interfaces. Cell Tissue Res. *358*, 843–855. https://doi.org/10.1007/s00441-014-1989-3.

Nakao, K., Morita, R., Saji, Y., Ishida, K., Tomita, Y., Ogawa, M., Saitoh, M., Tomooka, Y., and Tsuji, T. (2007). The development of a bioengineered organ germ method. Nat. Methods *4*, 227–230. https://doi.org/10.1038/nmeth1012.

Naveau, A., Zhang, B., Meng, B., Sutherland, M.T., Prochazkova, M., Wen, T., Marangoni, P., Jones, K.B., Cox, T.C., Ganss, B., et al. (2017). Isl1 controls patterning and mineralization of enamel in the continuously renewing mouse incisor. J. Bone Miner. Res. *32*, 2219–2231. https://doi.org/10.1002/jbmr.3202.

O'Sullivan, J., Bitu, C.C., Daly, S.B., Urquhart, J.E., Barron, M.J., Bhaskar, S.S., Martelli-Júnior, H., dos Santos Neto, P.E., Mansilla, M.A., Murray, J.C., et al. (2011). Whole-Exome sequencing identifies FAM20A mutations as a cause of amelogenesis imperfecta and gingival hyperplasia syndrome. Am. J. Hum. Genet. *88*, 616–620. https://doi.org/10.1016/j.ajhg.2011.04.005.

Paine, M.L., Wang, H.J., Luo, W., Krebsbach, P.H., and Snead, M.L. (2003). A transgenic animal model resembling amelogenesis imperfecta related to ameloblastin overexpression. J. Biol. Chem. *278*, 19447–19452. https://doi.org/10.1074/jbc.M300445200.

Pugach, M.K., and Gibson, C.W. (2014). Analysis of enamel development using murine model systems: approaches and limitations. Front. Physiol. *5*, 313. https://doi.org/10.3389/fphys.2014.00313.

Rawlings, T.M., Makwana, K., Taylor, D.M., Molè, M.A., Fishwick, K.J., Tryfonos, M., Odendaal, J., Hawkes, A., Zernicka-Goetz, M., Hartshorne, G.M., et al. (2021). Modelling the impact of decidual senescence on embryo implantation in human endometrial assembloids. Elife *10*, e69603. https://doi.org/10.7554/eLife.69603.

Rhodes, J.A., Fitzgibbon, D.H., Macchiarulo, P.A., and Murphy, R.A. (1987). Epidermal growth factor-induced precocious incisor eruption is associated with decreased tooth size. Dev. Biol. *121*, 247–252. https://doi.org/10.1016/0012-1606(87)90156-4.

Saito, K., Michon, F., Yamada, A., Inuzuka, H., Yamaguchi, S., Fukumoto, E., Yoshizaki, K., Nakamura, T., Arakaki, M., Chiba, Y., et al. (2020). Sox21 regulates Anapc10 expression and determines the fate of ectodermal organ. iScience *23*, 101329. https://doi.org/10.1016/j.isci.2020.101329.

Sanz-Navarro, M., Delgado, I., Torres, M., Mustonen, T., Michon, F., and Rice, D.P. (2019). Dental epithelial stem cells express the development regulator Meis1. Front. Physiol. *10*, 249. https://doi.org/10.3389/fphys.2019.00249.

Sarkar, J., Simanian, E.J., Tuggy, S.Y., Bartlett, J.D., Snead, M.L., Sugiyama, T., and Paine, M.L. (2014). Comparison of two mouse ameloblast-like cell lines for enamel-specific gene expression. Front. Physiol. *5*, 277. https://doi.org/10.3389/fphys.2014.00277.

Smith, C.E., and Warshawsky, H. (1977). Quantitative analysis of cell turnover in the enamel organ of the rat incisor. Evidence for ameloblast death immediately after enamel matrix secretion. Anat. Rec. *187*, 63–98. https://doi.org/10.1002/ar.1091870106.

Tsutsui, T.W. (2020). Dental pulp stem cells: advances to applications. Stem Cells Cloning. *13*, 33–42. https://doi.org/10.2147/SCCAA.S166759.

Vasconcelos, K.R., Arid, J., Evangelista, S., Oliveira, S., Dutra, A.L., Silva, L.A.B., Segato, R.A.B., Vieira, A.R., Nelson-Filho, P., and Küchler, E.C. (2019). MMP13 contributes to dental caries associated with developmental defects of enamel. Caries Res. *53*, 441–446. https://doi.org/10.1159/000496372.

Wazen, R.M., Viegas-Costa, L.C., Fouillen, A., Moffatt, P., Adair-Kirk, T.L., Senior, R.M., and Nanci, A. (2016). Laminin γ2 knockout mice rescued with the human protein exhibit enamel maturation defects. Matrix Biol. *52–54*, 207–218. https://doi.org/10.1016/j.matbio.2016.03.002.

Wee, P., and Wang, Z. (2017). Epidermal growth factor receptor cell proliferation signaling pathways. Cancers *9*, 52. https://doi.org/10.3390/cancers9050052.

Welborn, V.V. (2020). Enamel synthesis explained. Proc. Natl. Acad. Sci. USA *117*, 21847–21848. https://doi.org/10.1073/pnas.2014394117.

Xie, X., Liu, C., Zhang, H., Jani, P.H., Lu, Y., Wang, X., Zhang, B., and Qin, C. (2016). Abrogation of epithelial BMP2 and BMP4 causes Amelogenesis Imperfecta by reducing MMP20 and KLK4 expression. Sci. Rep. *6*, 25364. https://doi.org/10.1038/srep25364.

Yajima-Himuro, S., Oshima, M., Yamamoto, G., Ogawa, M., Furuya, M., Tanaka, J., Nishii, K., Mishima, K., Tachikawa, T., Tsuji, T., and Yamamoto, M. (2014). The junctional epithelium originates from the odontogenic epithelium of an erupted tooth. Sci. Rep. *4*, 4867. https://doi.org/10.1038/srep04867.

Stem Cell Reports, Volume *18*

Supplemental Information

Organoids from mouse molar and incisor as new tools to study tooth-specific biology and development

Florian Hermans, Lara Hemeryck, Celine Bueds, Marc Torres Pereiro, Steffie Hasevoets, Hiroto Kobayashi, Diether Lambrechts, Ivo Lambrichts, Annelies Bronckaers, and Hugo Vankelecom

Supplemental Figures and Legends

Figure S1

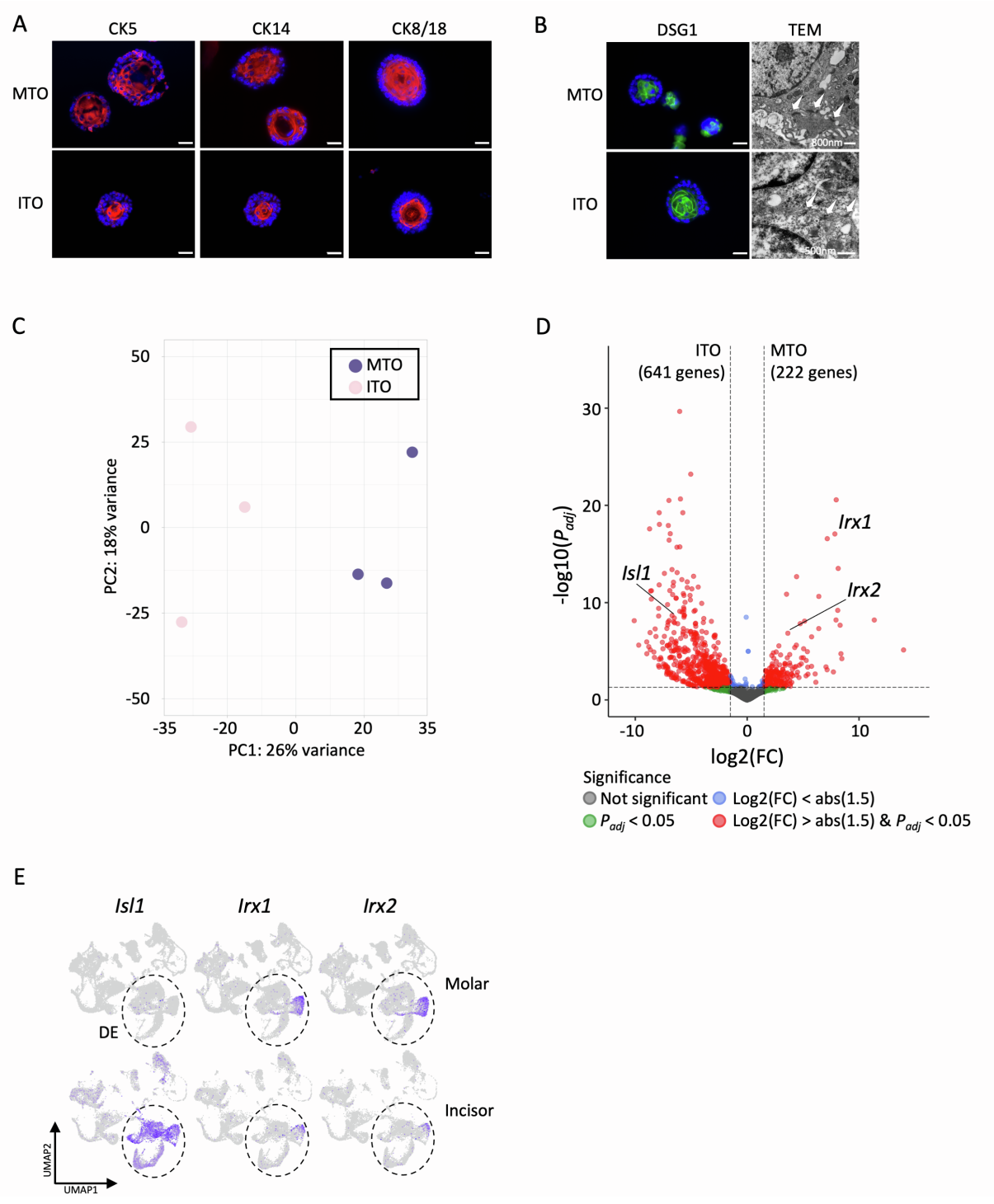

Figure S1. Additional characterization of organoids from mouse molar and incisor. Related to Figure 1. (A) IF analysis of indicated cytokeratins (CK; red) in TO. Nuclei of all IF images are counterstained with Hoechst33342. **(B)** IF (DSG1, green) and ultrastructural (TEM) characterization of desmosomes in TO. Arrows indicate desmosomes (TEM images). **(C)** PCA plot of bulk RNA-seq data from MTO and ITO (variance per component as indicated). **(D)** Volcano plot with log_2(fold change (FC)) *versus* -log10(P_{adj}) value) of RNA-seq data from MTO and ITO. Statistically upregulated genes (right for MTO and left for ITO) are indicated in red, as determined by a combination of log_2(FC) > the absolute (abs) value of ±1.5, and $P_{adj} < 0.05$. **(E)** Projection of indicated genes on our previously published mouse tooth scRNA-seq atlas (Hermans et al., 2022). The dental epithelium (DE) is circled. Scale bars: 25 μm for IF images.

Figure S2

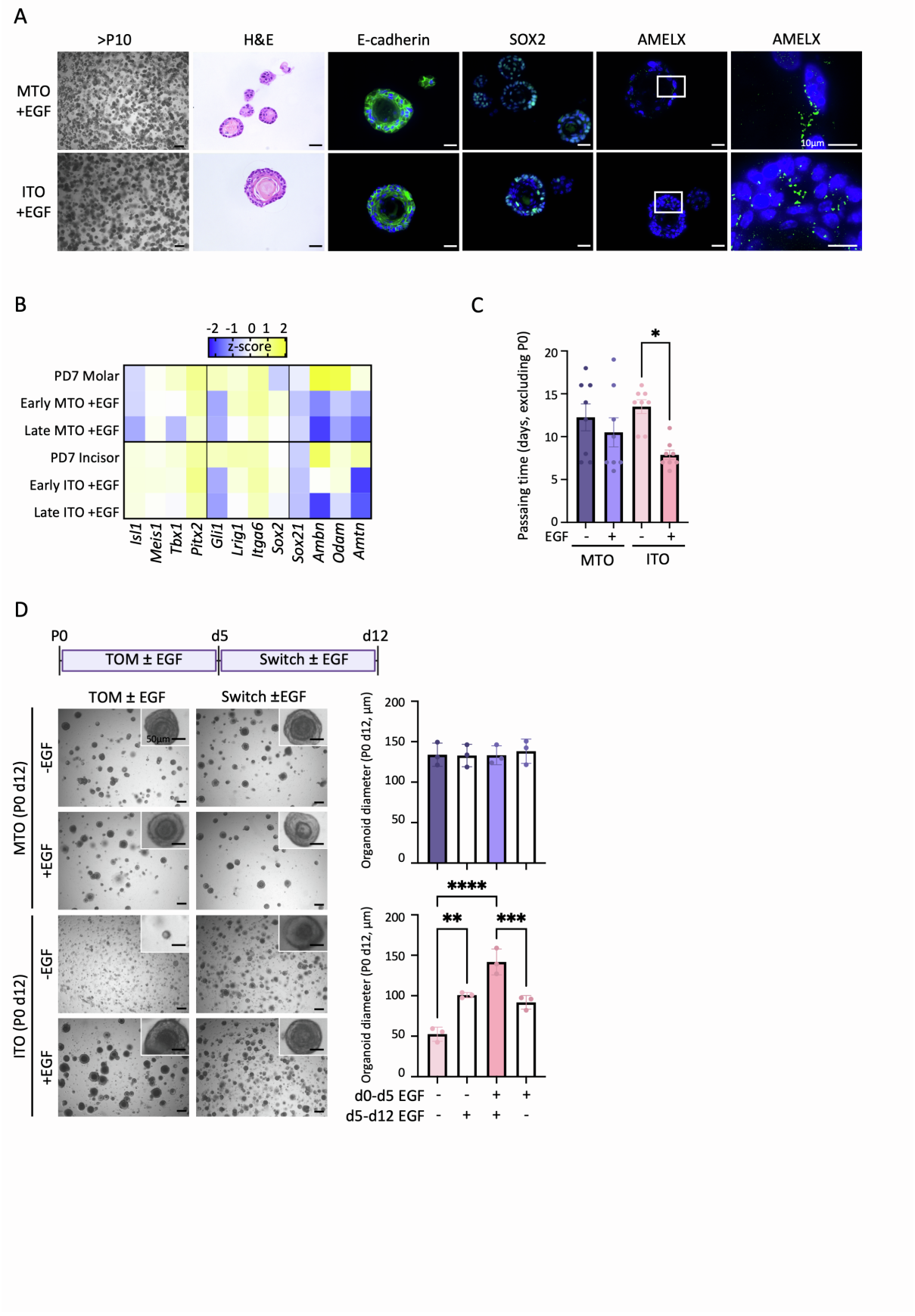
A
>P10
H&E
E-cadherin
SOX2
AMELX
AMELX
MTO +EGF
ITO +EGF
10µm
B
-2 -1 0 1 2
z-score
PD7 Molar
Early MTO +EGF
Late MTO +EGF
PD7 Incisor
Early ITO +EGF
Late ITO +EGF
Isl1
Meis1
Tbx1
Pitx2
Gli1
Lrig1
Itga6
Sox2
Sox21
Ambn
Odam
Amtn
C
Passaing time (days, excluding P0)
20
15
10
5
0
*
EGF - + - +
MTO
ITO
D
P0
d5
d12
TOM ± EGF
Switch ± EGF
TOM ± EGF
Switch ±EGF
50µm
MTO (P0 d12)
ITO (P0 d12)
-EGF
+EGF
-EGF
+EGF
Organoid diameter (P0 d12, µm)
200
150
100
50
0
****
**
***
d0-d5 EGF - - + +
d5-d12 EGF - + + -

Figure S2. Characterization of TO grown in the presence of exogenous EGF. Related to Figure 2. (A) Brightfield images of MTO and ITO grown in the presence of EGF after long-term culture for more than 10 passages (>P10); H&E and IF evaluation (of indicated markers) of organoid morphology and characteristics. Nuclei are counterstained with Hoechst33342 (blue). Boxed areas are magnified. **(B)** Heatmap of gene expression of DE TF, proposed DESC markers and EMP in primary molar and incisor tissue, early- and late-passage TO grown in the presence of EGF, as quantified by RT-qPCR analysis. Data are presented as relative expression to *Gapdh* (ΔC_t) and z-score normalized. Colors range from blue (low expression) to yellow (high expression). **(C)** Bar graph showing time between organoid passaging (days, excluding P0; mean ± SEM). Data points represent biological replicates from independently established organoid lines; one-way ANOVA with Šídák's multiple comparisons test. **(D)** *Top*: Timeline of experimental set-up. TO were seeded in P0 with or without EGF and grown for 12 days. After 5 days of initial growth in TOM with or without EGF, EGF was either removed or added from TOM ('switch'), respectively, for 7 more days. *Bottom-left***:** Brightfield images of P0 d12 organoids grown in TOM without exogenous EGF (-EGF) or with EGF (+EGF), or alternatively switched from -EGF to +EGF and *vice versa*. *Bottom-right*: Bar graphs (mean ± SEM) showing organoid diameter on d12. Data points represent biological replicates from independently established organoid lines; one-way ANOVA with Šídák's multiple comparisons test. Scale bars: 250 μm for brightfield images and 25 μm for H&E and IF images, unless indicated otherwise. **P* < 0.05, ***P* < 0.01, ****P* < 0.001, *****P* < 0.0001.

Figure S3

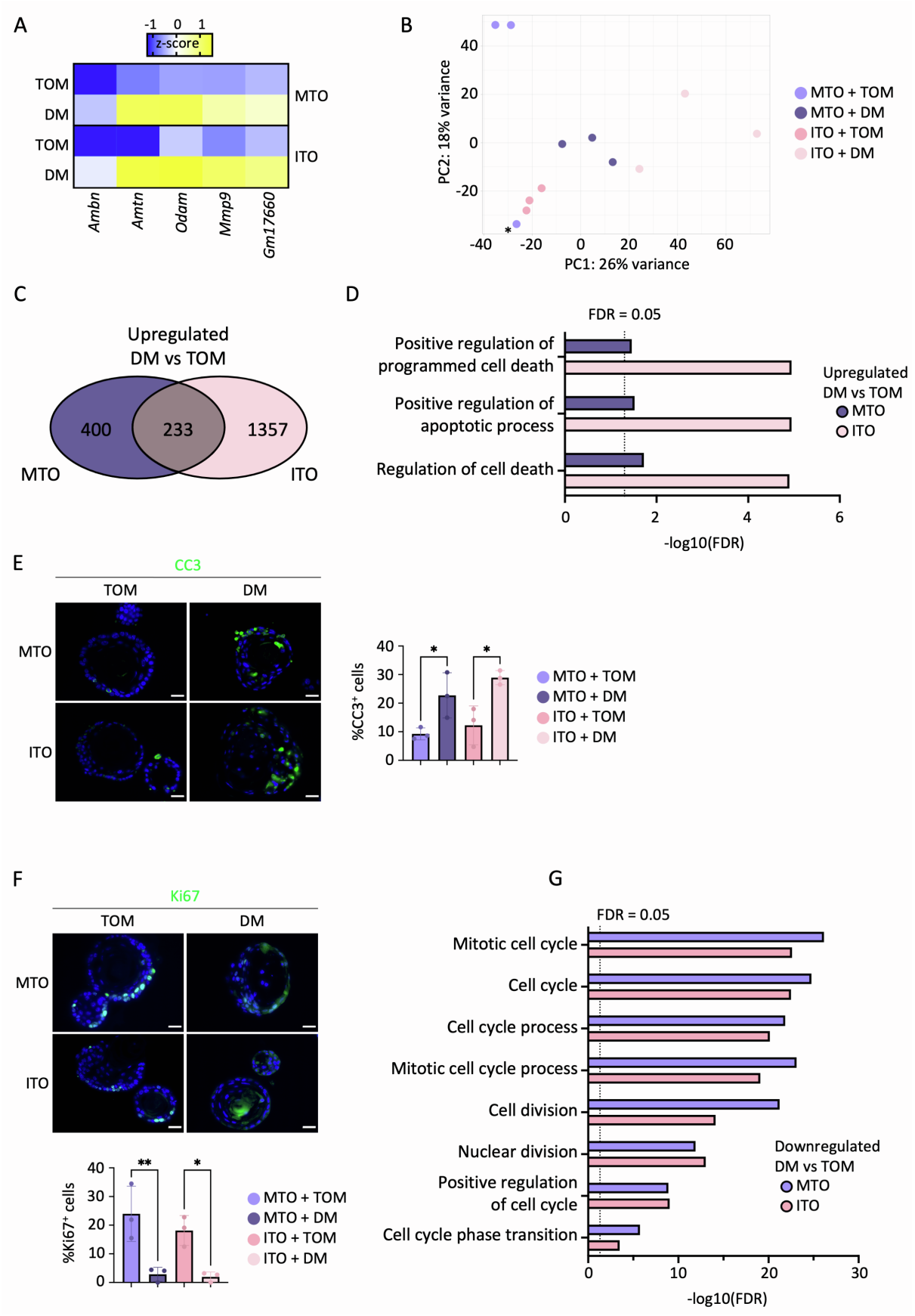
A
-1 0 1
z-score
TOM
DM
TOM
DM
MTO
ITO
Ambn
Amtn
Odam
Mmp9
Gm17660
B
PC2: 18% variance
PC1: 26% variance
MTO + TOM
MTO + DM
ITO + TOM
ITO + DM
C
Upregulated
DM vs TOM
400
233
1357
MTO
ITO
D
FDR = 0.05
Positive regulation of programmed cell death
Positive regulation of apoptotic process
Regulation of cell death
-log10(FDR)
Upregulated
DM vs TOM
MTO
ITO
E
CC3
TOM
DM
MTO
ITO
%CC3+ cells
MTO + TOM
MTO + DM
ITO + TOM
ITO + DM
F
Ki67
TOM
DM
MTO
ITO
%Ki67+ cells
MTO + TOM
MTO + DM
ITO + TOM
ITO + DM
G
FDR = 0.05
Mitotic cell cycle
Cell cycle
Cell cycle process
Mitotic cell cycle process
Cell division
Nuclear division
Positive regulation of cell cycle
Cell cycle phase transition
-log10(FDR)
Downregulated
DM vs TOM
MTO
ITO

Figure S3. *In vitro* differentiation of TO toward AB-resembling cells. Related to Figure 3. (A) Heatmap of gene expression of AB markers in TO grown in TOM or switched to DM after 7d, as quantified by RT-qPCR analysis. Data are presented as relative expression to *Gapdh* (ΔC_t) and z-score normalized. Colors range from blue (low expression) to yellow (high expression). **(B)** PCA plot of bulk RNA-seq data from TOM- and DM-grown MTO and ITO (variance per component as indicated). * indicates an outlier which was removed from subsequent analyses. **(C)** Venn diagram indicating the number of DEG upregulated in DM-*versus* TOM-grown MTO and ITO, and tooth-type overlap. **(D)** Significant (FDR ≤ 0.05, indicated by dotted line) DEG-based GO terms associated with apoptosis enriched in DM-grown TO compared to TOM-cultured controls. **(E)** *Left:* IF analysis of CC3 (green) in TO. Nuclei of all IF images are counterstained with Hoechst33342. *Right*: Bar graph (mean ± SEM) showing proportion of $CC3^+$ cells in organoids. Data points represent biological replicates from independently established organoid lines; one-way ANOVA with Šídák's multiple comparisons test. **(F)** *Top:* IF analysis of Ki67 (green) in TO. *Bottom*: Bar graph (mean ± SEM) showing proportion of $Ki67^+$ cells in organoids. Data points represent biological replicates from independently established organoid lines; one-way ANOVA with Šídák's multiple comparisons test. **(G)** Significant (FDR ≤ 0.05, indicated by dotted line) DEG-based GO terms associated with proliferation and cell cycle downregulated in DM-grown TO compared to TOM-cultured controls. Scale bars: 25 μm. *$P < 0.05$, **$P < 0.01$.

Figure S4

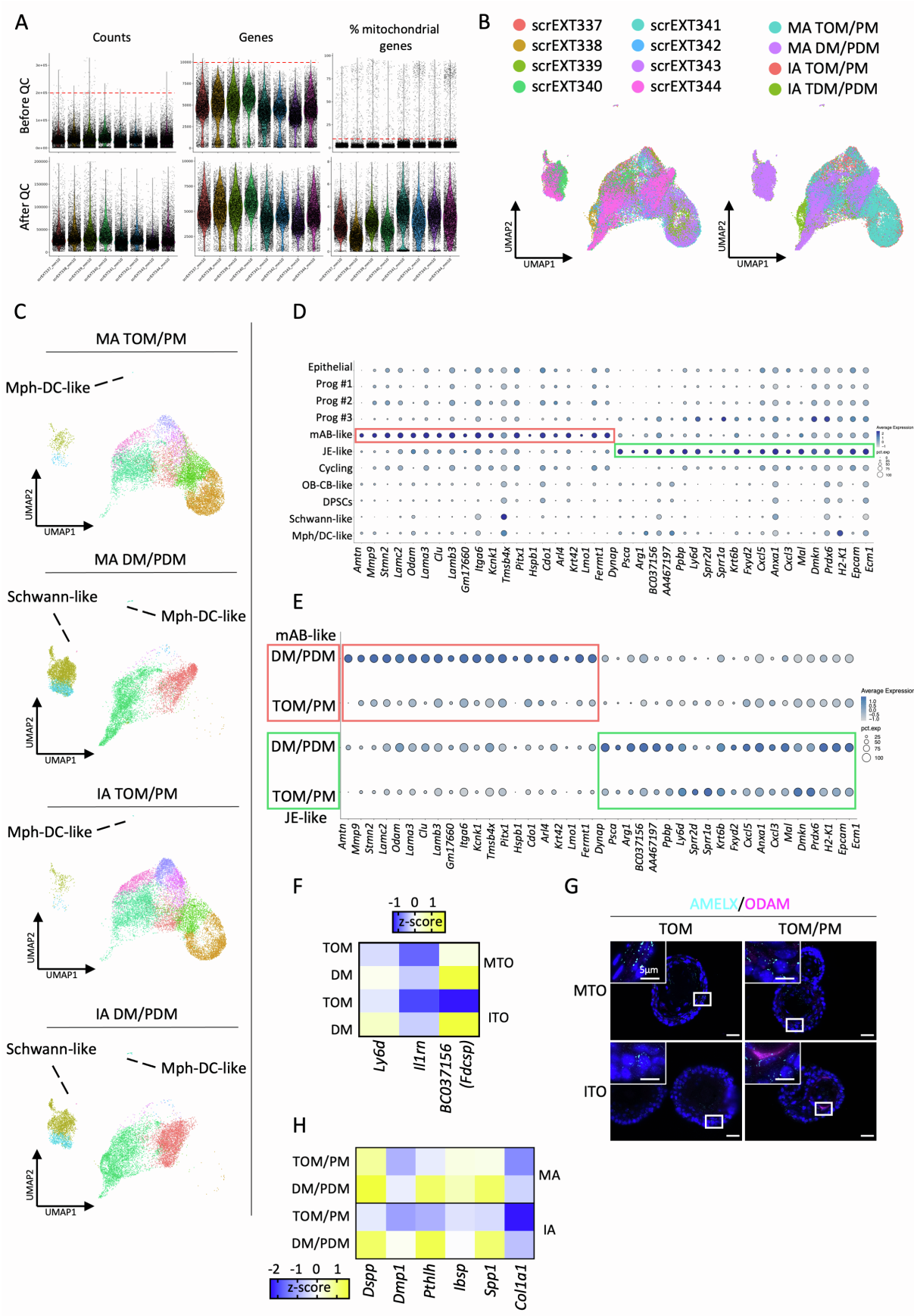
A
Counts
Genes
% mitochondrial genes
Before QC
After QC
B
scrEXT337
scrEXT338
scrEXT339
scrEXT340
scrEXT341
scrEXT342
scrEXT343
scrEXT344
MA TOM/PM
MA DM/PDM
IA TOM/PM
IA TDM/PDM
UMAP2
UMAP1
C
MA TOM/PM
Mph-DC-like
MA DM/PDM
Schwann-like
Mph-DC-like
IA TOM/PM
Mph-DC-like
IA DM/PDM
Schwann-like
Mph-DC-like
D
Epithelial
Prog #1
Prog #2
Prog #3
mAB-like
JE-like
Cycling
OB-CB-like
DPSCs
Schwann-like
Mph/DC-like
Amtn Mmp9 Stmn2 Lamc2 Odam Lama3 Clu Lamb3 Gm17660 Itga6 Kcnk1 Tmsb4x Pitx1 Hspb1 Cdo1 Arl4 Krt42 Lmo1 Fermt1 Dynap Psca Arg1 BC037156 AA467197 Ppbp Ly6d Sprr2d Sprr1a Krt6b Fxyd2 Cxcl5 Anxa1 Cxcl3 Mal Dmkn Prdx6 H2-K1 Epcam Ecm1
E
mAB-like
DM/PDM
TOM/PM
JE-like
Average Expression
pct.exp
F
z-score
TOM
DM
TOM
DM
MTO
ITO
Ly6d
Il1rn
BC037156 (Fdcsp)
G
AMELX/ODAM
TOM
TOM/PM
MTO
ITO
5μm
H
TOM/PM
DM/PDM
TOM/PM
DM/PDM
MA
IA
z-score
Dspp
Dmp1
Pthlh
Ibsp
Spp1
Col1a1

Figure S4. Quality control of tooth assembloid scRNA-seq analysis and additional characterization of developed assembloids. Related to Figure 4. (A) Violin plots showing the distribution of counts, genes and percent mitochondrial genes of the individual assembloid scRNA-seq samples before and after performing quality control (QC). Cells with values matching the following cut-offs were removed: counts >200,000, genes <1,000 and >10,000, percentage of mitochondrial genes >8%. **(B)** UMAP plots of integrated assembloid scRNA-seq data indicating individual samples (left, see Table S5) or experimental groups (right). **(C)** Annotated UMAP plots of integrated assembloid scRNA-seq datasets for MA TOM/PM- (*top*), MA DM/PDM- (*second*), IA TOM/PM- (*third*), and IA DM/PDM-grown (*bottom*) assembloids. See Figure 4C for cluster annotation. **(D)** Dotplot displaying the percentage of cells (dot size) expressing the top 20 DEG of mAB- (red box) and JE-like (green box) cells (average expression levels indicated by color intensity, see scale). **(E)** Dotplot displaying the percentage of mAB- (red) and JE-like (green) cells from TOM/PM- and DM/PDM-grown assembloids (dot size) expressing the top 20 DEG of mAB- (red box) and JE-like (green box) cells (average expression levels indicated by color intensity, see scale). **(F)** Heatmap of gene expression of JE markers in TO grown in TOM or switched to DM after 7d as quantified by RT-qPCR analysis (n=2 biological replicates from independently established organoid lines). Data are presented as relative expression to *Gapdh* (ΔC_t) and z-score normalized. Colors range from blue (low expression) to yellow (high expression). **(G)** IF analysis of AMELX (cyan) and ODAM (magenta) in TO controls grown in TOM or TOM/PM. Nuclei are counterstained with Hoechst33342 (blue). Boxed areas are magnified. **(H)** Heatmap of gene expression of markers of OB-/CB-like differentiation in tooth assembloids. Data are presented as relative expression to *Gapdh* (ΔC_t) and z-score normalized. Colors range from blue (low expression) to yellow (high expression). Scale bars: 25 μm, unless otherwise indicated.

Supplemental Tables

Table S1. Serum-free defined medium (SFDM) composition. Related to Table 1.

Product	Concentration	Supplier	Catalogue number
Sterile H_2O			
DMEM 1:1 F12 without Fe	16.8 g/L	Invitrogen	074-90715A
Bovine Serum Albumin (BSA)	5 g/L	Serva	47330.03
Catalase from bovine liver	50 μL/L	Sigma-Aldrich	C100
Ethanol absolute, ≥99.8%	600 μL/L	Fisher Chemical	E/0650DF/15
Insulin from bovine pancreas	5 mg/L	Sigma-Aldrich	I6634
$NaHCO_3$	1 g/L	Merck	106329
Penicillin	35 mg/L	Sigma-Aldrich	P3032
Streptomycin	50 mg/L	Sigma-Aldrich	S6501
Transferrin	5 mg/L	Serva	36760.01

Table S2. TO differentiation medium (DM) composition

Product	Concentration	Supplier	Catalogue number
SFDM			
B27 (without vitamin A)	2%	Gibco	12587-010
BMP2	100 ng/mL	Peprotech	120-02C
BMP4	50 ng/ML	Peprotech	120-05ET
EGF	20 ng/ML	R&D Systems	236-EG
FGF2 (=basic FGF)	20 ng/mL	R&D Systems	234-FSE
TGFβ1	4 ng/ML	R&D Systems	240-B

Table S3. Pulp medium (PM) composition

Product	Concentration	Supplier	Catalogue number
α-MEM		Sigma-Aldrich	M4526
ESGRO Recombinant LIF protein	10^3 units/mL	Sigma-Aldrich	ESG1107
Fetal Bovine Serum (FBS)	10 or 20%*	Sigma-Aldrich	F7524
FGF2 (=basic FGF)	2.5 ng/mL	R&D Systems	234-FSE
Penicillin-streptomycin	1%	Gibco	P4333

*20% FBS used for initial passage (i.e entire P0) of DPSC culture only. 10% FBS used for subsequent passages and all experiments.

Table S4. Pulp differentiation medium (PDM) composition

Product	Concentration	Supplier	Catalogue number
PM (with 10% FBS)			For composition see Table S3
Ascorbic acid	100 μM	Sigma-Aldrich	A4544
β-glycerophosphate	5 mM	Merck	35675-GM
Dexamethasone	10 μM	Sigma-Aldrich	D4902

Table S5. Metadata of assembloid scRNA-seq

Sample	Tooth derived	Condition	Medium
scrEXT337_mm10	Incisor	Control	TOM/PM
scrEXT338_mm10	Incisor	Differentiation	DM/PDM
scrEXT339_mm10	Molar	Control	TOM/PM
scrEXT340_mm10	Molar	Differentiation	DM/PDM
scrEXT341_mm10	Incisor	Control	TOM/PM
scrEXT342_mm10	Incisor	Differentiation	DM/PDM
scrEXT343_mm10	Molar	Control	TOM/PM
scrEXT344_mm10	Molar	Differentiation	DM/PDM

Table S6. Antibodies used for immunofluorescence staining

Primary antibodies

Antigen	Host	Company	Catalogue number	Dilution
AMELX	Mouse	Santa Cruz Biotechnology	365284	1:100
CC3	Rabbit	Sigma-Aldrich	AB3623	1:100
CK5	Rabbit	Biolegend	905501	1:1000
CK8/18	Guinea pig	Progen	GP11	1:200
CK14	Mouse	Thermo Fisher Scientific	MA5-11599	1:1000
DSG1	Rabbit	Proteintech	24587-1-ap	1:500
E-cadherin	Rabbit	Cell Signaling Technologies	24E10	1:400
ISL1	Rabbit	Abcam	ab20670	1:1000
Ki67	Mouse	BD Bioscience	556003	1:100
LAMC1	Rabbit	NovusBio (Biotechne)	NBP1-877118	1:200
ODAM	Rabbit	Proteintech	16509-I-AP	1:200
SOX2	Rabbit	Abcam	AB97959	1:2000
VIM	Rabbit	Cell Signaling Technologies	D21H3	1:400

Secondary antibodies

Antigen	Host	Company	Catalogue number	Dilution
Mouse IgG (A488)	Donkey	Thermo Fisher Scientific	A-21202	1:1000
Mouse IgG (A555)	Donkey	Thermo Fisher Scientific	A-31570	1:1000
Rabbit IgG (A488)	Donkey	Thermo Fisher Scientific	A-21206	1:1000
Rabbit IgG (A555)	Donkey	Thermo Fisher Scientific	A-31572	1:1000
Guinea pig IgG (FITC)	Donkey	Jackson Immunoresearch	706-096-148	1:500

Table S7. Forward and reverse primers used for qPCR gene expression analysis

Gene	Forward	Reverse
Ambn	CTGTCAACCAGGGAACCACT	TGTGATGCGGTTTAGCTGAG
Amtn	CTCAGACCGTCACATCCTCA	TGTGGATAAAGCAGGCTTCC
Areg	CCATCATCCTCGCAGCTATT	CTTGTCGAAGCCTCCTTCTT
BC037156 (Fdcsp)	AAAACTCTTCTCCTGCTCGCT	CACTGTCACTGGCACTTCGT
Btc	TTCGTGGTGGACGAGCAAACTC	CCATGACCACTATCAAGCAGACC
Col1a1	GCATGGCCAAGAAGACATCCC	GCATACCTCGGGTTTCCACG
Dmp1	CTCCTTGTGTTCCTTTGGGGG	TCTGATGACTCACTGTTCGTGG
Dspp	CAGGAACTGCAGCACAGAATGA	TATCTCACTGCCATCTGGGGA
Egf	ACTGGTGTGACACCAAGAGGTC	CCACAGGTGATCCTCAAACACG
Epgn	GAGCGAAGAAGCAGAGGTGATC	GGTCTTCCAGACAAGGATGAGAG
Ereg	CAGGCAGTTATCAGCACAACCG	CATGCAAGCAGTAGCCGTCCAT
Gapdh	ACCAGAGCATGATAAGGCAGCC	TGATGAGGCTGAAGGGTGTGAC
Gm17660	TTCCCGAATCTGTCGCTCC	TGGAACTTCCTCCGGATTGTC
Hbegf	GTCCGTCTGTCTTCTTGTCATC	CGCCCAACTTCACTTTCTCT
Ibsp	TACGGAGCAGAGACCACACC	TCTGCATCTCCAGCCTTCTTGG
Il1rn	GCTCATTGCTGGGTACTTACAA	CCAGACTTGGCACAAGACAGG
Isl1	GCTGCCTCTTTGATGGCTTCGA	CACATTCGGCACTGTTACAGCC
Itga6	CTCCTAATGCTATCTTCAAGGCG	ACCCTGAGATTGCCCAGAG
Lrig1	TTCAGCCAACGCTACCCTCACA	TAAGCCAGGTGATGCGTGGTGT
Ly6d	CAAAACCGTCACCTCAGTGGA	AGTCTGGCAGCATTGTGTGA
Meis1	GCAGTTGGCACAAGATACAGGAC	ACTGCTCGGTTGGACTGGTCTA
Mmp9	CTGGACAGCCAGACACTAAAG	CTCGCGGCAAGTCTTCAGAG
Nrg1	GCTCATCACTCCACGACTGTCA	TGCCTGCTGTTCTCTACCGATG
Nrg2	GGATGGCAAGGAACTCAACC	TCGGCCTCACAGACGTACT
Nrg3	CGAGACAAGGACCTGGCGTATT	TCACAACGGACTCCTTGGTAGC
Nrg4	TCCTCCTCACTCTTACCATCGC	GTCTCTACCAGGCTGATCTCAC
Odam	CCCTAAGATGCACAACTCGGAG	GTAGTCGGGATGCTCCTTCATG
Pitx2	CGGCAGAGGACTCATTTCAC	TTCTTGAACCAAACCCGGAC
Pthlh	GGCGTTCGGTGGAGGGGCTT	CAGATGGTGGAGGAAGAAACGG
Sox2	GAAGTGGCTGAACGAGGCATTG	TTGTCCGTGGAGGACCTTGCAT
Sox21	CCCTAAGATGCACAACTCGGAG	GTAGTCGGGATGCTCCTTCATG
Spp1	GGCAGCTCAGAGGAGAAGAAGC	AGCATTCTGTGGCGCAAGG
Tbx1	CGAGATGATCGTCACCAAGGCA	GTCATCTACGGGCACAAAGTCC

Supplemental experimental procedures

Isolation and dissociation of early-postnatal mouse molar and incisor tissue

C57BL/6 PD7 mice (pool of male and female) were used for tooth isolation, obtained by breeding in the Animal Housing Facility of the KU Leuven under conditions of constant temperature, humidity, 12-hour light-dark cycle and *ad libitum* access to food and water. Experiments were approved by the KU Leuven Ethical Committee for Animal Experimentation (P056/2022).

Pups were euthanized by decapitation, after which the mandibles were collected in Dulbecco's Modified Eagle Medium with 10 mM HEPES (DMEM; Gibco), supplemented with 10% fetal bovine serum (FBS; Sigma-Aldrich) and 1% penicillin-streptomycin (Gibco). Whole (unerupted) molars, including surrounding dental follicle and attached epithelium, as well as apical ends of (unerupted) incisors were carefully isolated, rinsed with phosphate-buffered saline (PBS; Gibco) and incubated with 2.5% Trypsin (Gibco) for 30 minutes at 37°C. Following trypsinization, the dental follicle and attached epithelium were manually recovered from the molars, and the dental pulp was separately collected from the molar pulp chamber. Subsequently, the molar (either dental follicle and attached epithelium or collected dental pulp tissue) and incisor tissues were further enzymatically digested with TrypLE Express (Gibco) supplemented with 5 µM ROCK inhibitor (ROCKi, Y-27632; Thermo Fisher) for 15 minutes at 37°C, and mechanically triturated (using syringes with decreasing diameters: 18G (Terumo), 20G (BD) and 26G (BD)) to a suspension containing single cells and small cell clusters. The number of collected cells was determined with a Z2 Coulter Particle Count and Size analyzer using COULTER Z2 AccuComp software (Beckman Coulter).

Establishment and passaging of mouse TO

The dissociated molar and incisor DE cell material was resuspended in serum-free defined medium (SFDM; Thermo Fisher Scientific; Table S1) and growth factor-reduced Matrigel (Corning) at a 30:70 ratio, supplemented with 10 µM ROCKi. Cells were seeded at 20,000 and 12,500 cells per 20 µL drop from molars and incisors, respectively. After solidification, pre-warmed TOM (Table 1) was added. Organoid cultures were kept at 37 °C in a 1.9% CO_2 incubator (as required by the SFDM buffering system), and medium was refreshed every 2 days. To passage the TO as occurring every 7-10 days, Matrigel droplets were collected using ice-cold SFDM, followed by incubation with TrypLE containing 5 µM ROCKi and mechanical trituration to dissociate the organoids. Remaining (large) organoid fragments were allowed to sediment, and the cell number in the supernatant, containing single cells and small fragments, was determined as described above. Upon reaching stable growth, dissociated MTO and ITO were seeded at 15,000-20,000 cells and 7,500 cells per 20 µL droplet, respectively. Organoids could be cryopreserved to be stored in liquid nitrogen, and be brought again in culture after thawing, all as previously described (Boretto et al., 2017; Cox et al., 2019).

To inhibit EGFR signaling, TO were treated with AG-1478 (1 µg/mL; Sigma-Aldrich) or EKI-785 (1 µM; Selleckchem) for 12 days from initial DE cell seeding. To explore TO differentiation capacity, organoids from passage 5 (P5) were grown in TOM for 7 days, and subsequently switched to culture in DM (Table S2) for 7 days. The DM was optimized by removing multiple growth factors from TOM one by one, and subsequently adding BMP2, BMP4 and TGFβ1. As initial readout for DM optimization, gene expression of EMP was assessed (*Ambn*, *Amtn*, *Odam*). Brightfield pictures of organoids were recorded using an Axiovert 40 CFL microscope (Zeiss).

DPSC culture

DPSC were obtained and cultured as previously described (Collignon et al., 2019). Briefly, molar pulp cells were seeded onto 0.1% gelatin-coated plates (gelatin from porcine skin; Sigma-Aldrich) and cultured in PM with 20% FBS (Table S3). Upon reaching 70-80% confluency, cells were dissociated using TrypLE and replated in PM with 10% FBS. The obtained DPSC were passaged every 7-10 days.

Establishment of mouse tooth assembloids

Tooth assembloids were established using a similar protocol as we previously described for human tooth assembloids (Hemeryck et al., 2022). Briefly, after dissociating TO (from P2-P3) and DPSC (from P2-P3), both matched and derived in the same tooth isolation experiment, into single cells as described above, both cell types were combined in round-bottom low-attachment plates (96-well; Greiner). Using a layered approach, 5,000 DPSC were first seeded by sedimentation (300 g for 1 min at 4 °C), followed by 5,000 MTO- or ITO-derived cells sedimented on top (300 g for 1 min at 4 °C) (Nakao et al., 2007). The cell composite was provided with 10% growth-factor reduced Matrigel and 90% of either a 1:1 mixture of TOM/PM or DM/PDM (Tables 1, S2-4). After 24 h incubation at 37 °C and 5% CO_2, the formed structures were collected and plated in 20 µL droplets of 70% Matrigel to generate tooth

assembloids which were maintained in the respective 1:1 media mixtures at 37 °C and 5% CO_2. Brightfield pictures of assembloids were recorded using an Axiovert 40 CFL microscope (Zeiss).

Histochemical and immunostaining analysis
Organoids were fixed in paraformaldehyde (PFA, 4% in PBS; Merck) for 30 min at room temperature (RT) and subsequently paraffin-embedded with an Excelsior ES Tissue Processor (Thermo Fisher Scientific). Paraffin sections of 5 µm thickness were obtained with a Microm HM 30 microtome (Thermo Fisher Scientific) and subjected to hematoxylin and eosin (H&E) or immunofluorescence (IF) staining. For IF analysis, antigen retrieval with citrate buffer (pH6; at 95°C) and permeabilization (0.1% Triton X-100; Sigma-Aldrich) were performed. For detection of ISL1, antigen retrieval was done with Tris-EDTA (pH9; at 95°C). Next, blocking buffer (0.15% glycine (VWR), 2 mg/mL BSA (Serva), 0.1% Triton-X in PBS) with 10% donkey serum (Sigma-Aldrich) was added for 1 h at RT. After incubation with primary antibodies and subsequently secondary antibodies (Table S6), and nuclei counterstaining with Hoechst33342 (1:1000; Merck), sections were mounted with ProLong Gold Antifade Mountant (Thermor Fisher Scientific). Images were recorded using a Leica DM5500 upright epifluorescence microscope (Leica Microsystems) accessible through the Imaging Core (VIB, KU Leuven), and analyzed and converted to pictures with Fiji imaging software. For visualization of $AMELX^+$ signals, the Fiji 'subtract background' function was used with a rolling ball radius of 3 pixels. Representative images are shown.

EdU labelling of TO
EdU labelling in TO was performed using the Click-iT EdU Alexa Fluor 488 kit (Thermo Fisher Scientific) according to the manufacturer's instructions, involving the incubation of organoids with EdU (10 µM) for 2 h. Images were recorded on a Zeiss LSM 780 – SP Mai Tai HP DS (Cell and Tissue Imaging Cluster (CIC), KU Leuven), and analyzed and converted to pictures with Fiji imaging software. Representative images are shown.

TEM analysis
Organoid samples were prepared for TEM as previously described in detail (Lambrichts et al., 1993; Cox et al., 2019). Samples were fixed in 2.5% glutaraldehyde (Sigma-Aldrich), dehydrated, embedded in epoxy resin, and cut into 40-70 nm sections. TEM images were acquired with the JEM1400 transmission electron microscope (JEOL) equipped with an Olympus SIS Quesmesa 11 Mpxl camera, or the Philips EM208 S electron microscope (Philips) equipped with the Morada Soft Imaging System camera with corresponding iTEM-FEI software (Olympus SIS), or a JEOL-1400 FLASH (JEOL) with Xarosa camera (EMSIS).

Gene expression analysis by qPCR
Total RNA was extracted from dissociated molar and incisor tissue, TO and tooth assembloids using the GenElute Mammalian Total RNA Miniprep kit (Sigma-Aldrich) following manufacturer's instructions. RNA was reverse-transcribed (RT) using the Superscript III First-Strand Synthesis Supermix kit (Thermo Fisher Scientific). The resultant cDNA samples were analyzed with SYBR Green-based quantitative (q)PCR with the Platinum SYBR Green qPCR SuperMix-UDG kit (Invitrogen) and using specific forward and reverse primers (Table S7), as described before (Cox et al., 2019). Glyceraldehyde-3-phosphate dehydrogenase (*Gapdh)* was included as housekeeping gene. Gene expression levels were calculated as ΔCt values relative to *Gapdh* ($Ct_{target} - Ct_{housekeeping}$). Z-score normalization was performed by subtracting the mean ΔCt of the experiment and dividing by the standard deviation of the obtained ΔCt values for each measurement.

Bulk RNA-seq analysis
RNA was isolated from P0 MTO and ITO grown in TOM (n=3 biological replicates per condition), or from P5 MTO and ITO grown in TOM+EGF and exposed to DM or not (n=3 biological replicates per condition). Total RNA was isolated using the GenElute Mammalian Total RNA Miniprep kit (Sigma-Aldrich) following manufacturer's instructions, and RNA Integrity Number (RIN) determined with Agilent Picochips on an Agilent BioAnalyzer 2100 (Agilent Technologies). Samples with RIN > 7.5 were sequenced (Nucleomics Core, VIB/KU Leuven). TruSeq total stranded RNA library preparation was performed, followed by sequencing on a NovaSeq 6000 instrument (Illumina). Data are accessible from ArrayExpress database (accession number E-MTAB-12557). Following quality control, reads were aligned to the mouse reference genome (*Mus musculus*, GRCm38/mm10 release M21) and transcript abundancies were quantified using Salmon (1.4.0) (Patro et al., 2017). Gene-level count matrices were created using the tximport package (v1.18.0) and used as input for DEG analysis with DESeq2 (v1.30.1) as previously reported (Love et al., 2014; Soneson et al., 2016). PCA analysis was performed using the

plotPCA function from the DESeq2 package after rlog transformation. Based on PCA analysis, one MTO+TOM sample was considered an outlier and omitted from further downstream analyses. For visualization and gene ranking, log fold change (LFC) estimates were shrunk using the apeglm (v1.12.0) method for effect size shrinkage as described (Love et al., 2014; Zhu et al., 2019). Volcano plots were generated using the EnhancedVolcano package (v1.6.0) (https://github.com/kevinblighe/EnhancedVolcano). GO analysis (FDR < 0.05) of DEG ($log_2FC > 1.5$ and *P*adj < 0.05) was executed with the GO webplatform (www.geneontology.org) (Ashburner et al., 2000; Carbon et al., 2021). Enriched pathway values are presented as $-log_{10}$(FDR).

scRNA-seq analysis

MA and IA, exposed to DM or not (2 replicates per condition), were dissociated into single cells using 0.25% Trypsin (Gibco; supplemented with 5μM ROCKi) treatment and mechanical trituration, collected in 0.04% BSA (in PBS) and filtered through a Flowmi 40 μm cell strainer (Sigma-Aldrich). Single cells were loaded onto 10X Genomics cartridge according to the manufacturer's instructions. Generation of barcoded libraries was performed with the Chromium Single-cell 3' v2 Chemistry Library Kit, Gel Bead & Multiplex Kit and Chip Kit (10× Genomics). The libraries were sequenced on an Illumina NextSeq and NovaSeq6000. Data are accessible from ArrayExpress database (accession number E-MTAB-12544). Raw sequencing reads were demultiplexed, mapped to the mouse reference genome (mm10) and gene expression matrices were generated using CellRanger (v5.0.0; 10× Genomics).

Downstream analysis was performed in Seurat (v4.0.0) as previously described (Stuart et al., 2019; Hao et al., 2021; Hermans et al., 2022). Briefly, low quality cells and potential doublets were removed based on the number of counts (>200,000) and genes (<1,000 and >10,000) per cell, as well as the percentage of mitochondrial genes (>8%) expressed per cell. After quality control, data were normalized and variable features identified (using the NormalizeData and FindVariableFeatures functions), and the data were integrated by the combination of tooth type and medium condition (i.e. MA+TOM/PM, MA+DM/PDM, IA+TOM/PM and IA+DM/PDM) using the FindIntegrationAnchors (with default parameters and dims = 1:30) and the IntegrateData functions. After scaling of expression levels, integrated data were subjected to PCA. Uniform Manifold Approximation and Projection (UMAP) dimensionality reduction was performed (with umap.method=uwot, using the top 50 PC and with min.dist=0.5). Initial clustering and annotation were performed, prior to correction of count matrices for ambient/background RNA using the SoupX (v1.5.0) package (Young and Behjati, 2020). The global contamination fractions were estimated to be 1.7%, well within normal range (0–10%).

Using the SoupX corrected counts, data were integrated using the reciprocal PCA (rPCA) method (Hao et al., 2021). Therefore, after data normalization and identification of variable features, each individual dataset was scaled and subjected to PCA analysis, which was used as input to the FindIntegrationAnchors function (with dims=1:30 and reduction='rpca') after which the datasets were integrated across all features using the IntegrateData function. During the scaling of the data, cell cycle regression was performed. Lists of human S and G2M genes were obtained from Seurat and converted to their mouse orthologues as input for the CellCycleScoring function. Following integration, the dataset was subjected to PCA, after which the top 50 PC were used for UMAP dimensionality reduction (with umap.method=uwot and min.dist=0.5) and clustering. Clustering and annotation were finalized using resolution 1.2 and 50 (to allow separation of the Schwann-like cluster) and evaluation of marker expression. DEG analysis between AB-like and JE-like clusters was performed in Seurat with the SoupX-corrected counts using the FindMarkers function with logfc.threshold=0.5 and min.pct=0.5.

Subcutaneous transplantation of ITO

Matrigel with d7 ITO (P5) was pipetted into custom-made 3D-printed hydroxyapatite scaffolds (Sirris) which were s.c. transplanted in immunodeficient nu/nu mice (Janvier Labs), as in detail described elsewhere (Bronckaers et al., 2021; Hemeryck et al., 2022). Scaffolds with only Matrigel were used as negative controls. One week later, implants were resected, and grafts carefully extracted and fixed in 4% PFA before processing for H&E or IF staining as described above. This study was approved by the Ethical Committee on Animal Experiments (ECAE) of UHasselt (protocol 202138).

Chicken CAM assay

Fertilized chicken eggs (*gallus gallus*) were incubated for 3 days at 37 °C and constant humidity. Next, 3 ml of albumen was removed and eggs were again incubated until embryonic day (E) 9 as previously in detail described (Bronckaers et al., 2013). Subsequently, pre-solidified 30 µl Matrigel droplets with d7 ITO (P5) were applied onto the CAM following the creation of a 1 cm^2 window into the shell to expose the CAM. Droplets of Matrigel alone served as negative controls. The window was covered with

cellophane tape and eggs were returned to the incubator. One week later, the CAM was removed and fixed in 4% PFA for H&E and IF analysis (described above).

Statistical analysis

Statistical analyses were performed using GraphPad Prism (v9.3.1) for macOS and are specified in the figure legends. All experiments were performed with ≥ 3 independent biological replicates (i.e. organoid lines established from independent mouse litters) unless otherwise indicated.

Supplemental references

Ashburner, M., Ball, C. A., Blake, J. A., Botstein, D., Butler, H., Cherry, J. M., et al. (2000). Gene Ontology: tool for the unification of biology. *Nat Genet* 25, 25–29. doi: 10.1038/75556.

Boretto, M., Cox, B., Noben, M., Hendriks, N., Fassbender, A., Roose, H., et al. (2017). Development of organoids from mouse and human endometrium showing endometrial epithelium physiology and long-term expandability. *Development* 144, 1775–1786. doi: 10.1242/dev.148478.

Bronckaers, A., Hilkens, P., Fanton, Y., Struys, T., Gervois, P., Politis, C., et al. (2013). Angiogenic Properties of Human Dental Pulp Stem Cells. *PLoS One* 8, e71104. doi: 10.1371/journal.pone.0071104.

Bronckaers, A., Hilkens, P., Wolfs, E., and Lambrichts, I. (2021). "By the Skin of Your Teeth: A Subcutaneous Mouse Model to Study Pulp Regeneration," in *Vascular Morphogenesis. Methods in Molecular Biology*, ed. D. Ribatti (Humana Press Inc.), 223–232. doi: 10.1007/978-1-0716-0916-3_16.

Carbon, S., Douglass, E., Good, B. M., Unni, D. R., Harris, N. L., Mungall, C. J., et al. (2021). The Gene Ontology resource: enriching a GOld mine. *Nucleic Acids Res* 49, D325–D334. doi: 10.1093/nar/gkaa1113.

Collignon, A. M., Castillo-Dali, G., Gomez, E., Guilbert, T., Lesieur, J., Nicoletti, A., et al. (2019). Mouse Wnt1-CRE-RosaTomato Dental Pulp Stem Cells Directly Contribute to the Calvarial Bone Regeneration Process. *Stem Cells* 37, 701–711. doi: 10.1002/stem.2973.

Cox, B., Laporte, E., Vennekens, A., Kobayashi, H., Nys, C., Van Zundert, I., et al. (2019). Organoids from pituitary as a novel research model toward pituitary stem cell exploration. *Journal of Endocrinology* 240, 287–308. doi: 10.1530/JOE-18-0462.

Hao, Y., Hao, S., Andersen-Nissen, E., Mauck, W. M., Zheng, S., Butler, A., et al. (2021). Integrated analysis of multimodal single-cell data. *Cell* 184, 3573-3587.e29. doi: 10.1016/j.cell.2021.04.048.

Hemeryck, L., Hermans, F., Chappell, J., Kobayashi, H., Lambrechts, D., Lambrichts, I., et al. (2022). Organoids from human tooth showing epithelial stemness phenotype and differentiation potential. *Cellular and Molecular Life Sciences* 79, 153. doi: 10.1007/s00018-022-04183-8.

Hermans, F., Bueds, C., Hemeryck, L., Lambrichts, I., Bronckaers, A., and Vankelecom, H. (2022). Establishment of inclusive single-cell transcriptome atlases from mouse and human tooth as powerful resource for dental research. *Front Cell Dev Biol* 10, 1021459. doi: 10.3389/fcell.2022.1021459.

Lambrichts, I., Creemers, J., and Van Steenberghe, D. (1993). Periodontal neural endings intimately relate to epithelial rests of Malassez in humans. A light and electron microscope study. *J Anat* 182, 153.

Love, M. I., Huber, W., and Anders, S. (2014). Moderated estimation of fold change and dispersion for RNA-seq data with DESeq2. *Genome Biol* 15, 550. doi: 10.1186/s13059-014-0550-8.

Nakao, K., Morita, R., Saji, Y., Ishida, K., Tomita, Y., Ogawa, M., et al. (2007). The development of a bioengineered organ germ method. *Nat Methods* 4, 227–230. doi: 10.1038/nmeth1012.

Patro, R., Duggal, G., Love, M. I., Irizarry, R. A., and Kingsford, C. (2017). Salmon provides fast and bias-aware quantification of transcript expression. *Nat Methods* 14, 417–419. doi: 10.1038/nmeth.4197.

Soneson, C., Love, M. I., and Robinson, M. D. (2016). Differential analyses for RNA-seq: transcript-level estimates improve gene-level inferences. *F1000Res* 4, 1521. doi: 10.12688/f1000research.7563.2.

Stuart, T., Butler, A., Hoffman, P., Hafemeister, C., Papalexi, E., Mauck, W. M., et al. (2019). Comprehensive Integration of Single-Cell Data. *Cell* 177, 1888-1902.e21. doi: 10.1016/j.cell.2019.05.031.

Young, M. D., and Behjati, S. (2020). SoupX removes ambient RNA contamination from droplet-based single-cell RNA sequencing data. *Gigascience* 9, giaa151. doi: 10.1093/gigascience/giaa151.

Zhu, A., Ibrahim, J. G., and Love, M. I. (2019). Heavy-tailed prior distributions for sequence count data: removing the noise and preserving large differences. *Bioinformatics* 35, 2084–2092. doi: 10.1093/bioinformatics/bty895.